



Universiteit  
Leiden  
The Netherlands

## The NuSTAR and Chandra view of CL 0217+70 and Its tell-tale radio halo

Tümer, A.; Wik, D.R.; Zhang, X.; Hoang, D.N.; Gaspari, M.; Weeren, R.J. van; ... ; Plaa, J. de

### Citation

Tümer, A., Wik, D. R., Zhang, X., Hoang, D. N., Gaspari, M., Weeren, R. J. van, ... Plaa, J. de. (2023). The NuSTAR and Chandra view of CL 0217+70 and Its tell-tale radio halo. *The Astrophysical Journal*, 942(2). doi:10.3847/1538-4357/aca1b5

Version: Publisher's Version












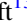
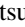

License: [Creative Commons CC BY 4.0 license](https://creativecommons.org/licenses/by/4.0/)

Downloaded from: <https://hdl.handle.net/1887/3716940>

**Note:** To cite this publication please use the final published version (if applicable).



# The NuSTAR and Chandra View of CL 0217+70 and Its Tell-tale Radio Halo

Ayşegül Tümer<sup>1,2</sup> , Daniel R. Wik<sup>1</sup> , Xiaoyuan Zhang<sup>3,4</sup> , Duy N. Hoang<sup>5</sup> , Massimo Gaspari<sup>6</sup> , Reinout J. van Weeren<sup>3</sup> , Lawrence Rudnick<sup>7</sup> , Chiara Stuardi<sup>8,9</sup> , François Mernier<sup>10</sup> , Aurora Simionescu<sup>4,11,12</sup> , Randall A. Rojas Bolivar<sup>1</sup> , Ralph Kraft<sup>13</sup> , Hiroki Akamatsu<sup>4</sup> , and Jelle de Plaa<sup>4</sup> 

<sup>1</sup> Department of Physics & Astronomy, The University of Utah, 115 South 1400 East, Salt Lake City, UT 84112, USA; [aysegultumer@gmail.com](mailto:aysegultumer@gmail.com)

<sup>2</sup> Kavli Institute for Astrophysics and Space Research, Massachusetts Institute of Technology, 77 Massachusetts Avenue, Cambridge, MA 02139, USA

<sup>3</sup> Leiden Observatory, Leiden University, PO Box 9513, 2300 RA Leiden, The Netherlands

<sup>4</sup> SRON Netherlands Institute for Space Research, Sorbonnelaan 2, 3584 CA Utrecht, The Netherlands

<sup>5</sup> Hamburger Sternwarte, University of Hamburg, Gojenbergsweg 112, D-21029 Hamburg, Germany

<sup>6</sup> Department of Astrophysical Sciences, Princeton University, 4 Ivy Lane, Princeton, NJ 08544-1001, USA

<sup>7</sup> Minnesota Institute for Astrophysics, University of Minnesota, 116 Church St.S.E., Minneapolis, MN 55455, USA

<sup>8</sup> Dipartimento di Fisica e Astronomia, Università di Bologna, via Gobetti 93/2, I-40129 Bologna, Italy

<sup>9</sup> INAF—Istituto di Radioastronomia di Bologna, Via Gobetti 101, I-40129 Bologna, Italy

<sup>10</sup> European Space Agency (ESA), European Space Research and Technology Centre (ESTEC), Keplerlaan 1, 2201 AZ Noordwijk, The Netherlands

<sup>11</sup> Leiden Observatory, Leiden University, PO Box 9513, NL-2300 RA Leiden, The Netherlands

<sup>12</sup> Netherlands Institute for Radio Astronomy (ASTRON), P.O. Box 2, 7990 AA Dwingeloo, The Netherlands

<sup>13</sup> Harvard-Smithsonian Center for Astrophysics, 60 Garden Street, Cambridge, MA 02138, USA

Received 2022 June 18; revised 2022 October 26; accepted 2022 November 8; published 2023 January 13

## Abstract

Mergers of galaxy clusters are the most energetic events in the universe, driving shock and cold fronts, generating turbulence, and accelerating particles that create radio halos and relics. The galaxy cluster CL 0217+70 is a remarkable late-stage merger, with a double peripheral radio relic and a giant radio halo. Chandra detects surface brightness (SB) edges that correspond to radio features within the halo. In this work, we present a study of this cluster with Nuclear Spectroscopic Telescope Array and Chandra data using spectro-imaging methods. The global temperature is found to be  $kT = 9.1$  keV. We set an upper limit for the inverse Compton (IC) flux of  $\sim 2.7 \times 10^{-12}$  erg s<sup>-1</sup> cm<sup>-2</sup>, and a lower limit to the magnetic field of 0.08  $\mu$ G. Our local IC search revealed a possibility that IC emission may have a significant contribution at the outskirts of the radio halo emission and on/near shock regions within  $\sim 0.6 r_{500}$  of clusters. We detected a “hot spot” feature in our temperature map coincident with an SB edge, but our investigation on its origin is inconclusive. If the “hot spot” is the downstream of a shock, we set a lower limit of  $kT > 21$  keV to the plasma that corresponds to  $\mathcal{M} \sim 2$ . We found three shock fronts within  $0.5 r_{500}$ . Multiple weak shocks within the cluster center hint at an ongoing merger activity and continued feeding of the giant radio halo. CL 0217+70 is the only example hosting these secondary shocks in multiple form.

*Unified Astronomy Thesaurus concepts:* Galaxy clusters (584); Shocks (2086); High energy astrophysics (739); Intracluster medium (858); Non-thermal radiation sources (1119)

## 1. Introduction

Galaxy clusters are the largest gravitationally bound structures in the universe, which contain hundreds of galaxies within a radius of 12 Mpc (Abell 1958). The intracluster medium (ICM) is an optically thin hot plasma ( $\sim 10^7$ – $10^8$  K) in X-rays that fills in between the galaxies inside galaxy clusters.

Mergers between galaxy clusters are the most energetic ( $10^{63}$ – $10^{64}$  ergs) events in the universe since the Big Bang. These mergers drive shocks that heat and mix the thermal gas while also (re)accelerating electrons and cosmic rays through Fermi-like acceleration processes across shocks and turbulent eddies (Brunetti & Jones 2014). Turbulence is a common phenomenon in the ICM, recurrently driven by mergers at large scales (e.g., Gaspari & Churazov 2013; Eckert et al. 2017), sustained by active galactic nuclei (AGN) feedback (e.g., Gaspari 2015; Hofmann et al. 2016; Yang et al. 2019; Wittor & Gaspari 2020) and ram-pressure stripping processes at small scales (e.g., De Grandi et al. 2016; Clavico et al. 2019).

The ICM carries the X-ray traces of mergers such as shock fronts that are detected as spatial variations in the temperature and density (see, e.g., Markevitch et al. 1999, and references therein). While surface brightness (SB) edges hint at the existence of a shock or cold front, temperature measurements at both sides of the SB edges can distinguish these two scenarios. Shocks caused by mergers have relatively low Mach numbers,  $\mathcal{M} \lesssim 3$  (see, e.g., Gabici & Blasi 2003; Ryu et al. 2003).

Mergers also produce relativistic particles emitting via nonthermal synchrotron process that can be detected by radio observations. The diffuse radio emission can be in the form of radio relics and radio halos. Relics are defined as extended radio emission features that are not associated with an active cluster radio galaxy or central region of a galaxy cluster (Giovannini & Feretti 2004). They are located at the peripheries of clusters and are characterized by polarized radio emission with steep spectra and elongated shapes (Ensslin et al. 1998). So far,  $\sim 45$  clusters are known to host these structures and almost as many candidates (van Weeren et al. 2019). Double radio relic systems, where relics appear on opposing sides of the cluster, are even rarer. Seventeen such systems are known to date, and only seven of them host giant radio halos (van Weeren et al. 2019).



Original content from this work may be used under the terms of the [Creative Commons Attribution 4.0 licence](https://creativecommons.org/licenses/by/4.0/). Any further distribution of this work must maintain attribution to the author(s) and the title of the work, journal citation and DOI.

**Table 1**  
Observation Log

	Observation ID	Start Date (yyyy-mm-dd)	Equatorial Coordinates (J2000)	Effective Exposure (ks)
NuSTAR	70701001002	2021-07-04	02:16:58.2 + 70:36:48	~230
	70701001004	2021-07-08	02:17:06.9 + 70:37:05	~106
Chandra	16293	2014-12-01	02:16:49.00 + 70:35:52.00	~25

Radio halos are megaparsec-scale structures that are found at the center of dynamically disturbed clusters with large-scale particle acceleration processes (Cassano et al. 2010; Feretti et al. 2012), yet they are not ubiquitous (Schellenberger et al. 2019). While evidence suggests that radio relics trace shock fronts from the initial collisions of clusters, the origin of radio halos is less clear (see, e.g., Brunetti et al. 2012). The prevailing view is that the relativistic electrons producing radio halos are accelerated by turbulence in the ICM.

Unlike relics, most radio halos have no known shock front–radio emission edge connection except for a few cases, e.g., Abell 520 (Hoang et al. 2019), the Toothbrush (van Weeren et al. 2016), the Coma Cluster (Brown & Rudnick 2011; Planck Collaboration et al. 2013), the Bullet Cluster (Shimwell et al. 2014), and Abell 2146 (Hlavacek-Larrondo et al. 2017). This small number of cluster mergers with known shock front–radio edge connection suggests that turbulence formed directly behind shocks is what accelerates the electrons in radio halos, whether from the initial collision or a subsequent settling of the ICM. The Bullet Cluster may be an example of the former case (initial collision), since its radio halo extends right up to the bow shock-driven by the subcluster’s first core passage (Shimwell et al. 2014). In contrast, the Coma cluster seems to be the only example of the latter scenario (subsequent settling of the ICM) so far. Recent eROSITA images, combined with Sunyaev–Zeldovich (SZ) and radio data, convincingly illustrate the formation and connection to a radio halo edge of a secondary shock (Zhang et al. 2020a). This secondary shock was also detected in X-rays by Simionescu et al. (2013).

In addition, the same relativistic electrons producing the synchrotron-powered radio halo also upscatter cosmic microwave background (CMB) photons to X-ray energies. The ratio of fluxes between the synchrotron and this inverse Compton (IC) emission is simply the ratio of the energy densities of their respective radiation fields: the magnetic field strength  $B$  and the CMB, respectively (Wik et al. 2014). Since the latter is very well known, an IC detection or upper limit directly leads to an estimate or lower limit on the volume-averaged value of  $B$ , a quantity that is poorly constrained in galaxy clusters generally.

Past Nuclear Spectroscopic Telescope Array (NuSTAR) searches for IC emission (see, e.g., Wik et al. 2011, 2014; Cova et al. 2019; Rojas Bolivar et al. 2021) constrain  $B \gtrsim 0.1\text{--}0.2 \mu\text{G}$ , comparable to the strength estimated from IC detections made with RXTE and BeppoSAX. Those detections remain controversial, but if IC emission could be definitively measured in a cluster, implying  $B \sim 0.1 \mu\text{G}$ , the dynamical role of magnetic fields in clusters would be confirmed to be negligible, as is currently assumed in simulations and mass scaling relations used in cluster cosmology (see, e.g., Vikhlinin et al. 2009).

One of these rare double radio relic systems at  $z=0.18$  (Zhang et al. 2020b) is CL 0217+70. This cluster hosts the most extended (3.5 Mpc) radio relic known accompanied by a giant radio halo with the largest projected distance of

1.5–1.8 Mpc (Brown et al. 2011; Hoang et al. 2021). Its two radio relics are mostly separated from its radio halo and lie at a large projected distance, indicating the first core passage was not recent. Intriguingly, two X-ray SB discontinuities or edges have recently been reported from a 25 ks Chandra observation (Zhang et al. 2020b), which are roughly coincident with spectral edges in the radio halo, i.e., locations where the spectral index suddenly changes from flat to steep, suggesting a transition to a zone of particle acceleration (Hoang et al. 2021). However, the nature of these X-ray SB edges are unknown. A confirmation that at least one of these edges is a shock front would add CL 0217+70 to a rare class of objects with the potential to unravel how particles in radio halos are accelerated.

In addition, the Chandra image of CL 0217+70 exhibits a  $1'$  wide SB depression, or “channel” (Zhang et al. 2020b). Such structures can only exist if they are supported by some form of nonthermal pressure: a locally enhanced value of either  $P_B$  or of the density of nonthermal particles. The former case would suppress all X-ray emission, while the latter case would lead to enhanced IC emission, more easily detected at hard X-ray energies.

In this work, we study CL 0217+70 using recent NuSTAR and archival Chandra data to study the nature of these SB edges, as well as searching for global and local IC emission.

The paper is organized as follows. Observations, the data-reduction process, and the background assessment of the NuSTAR data are presented in Section 2. In Section 3, methods used for the various analyses of the cluster and their respective results are presented. We discuss our findings in Section 4, and present our conclusions in Section 5.

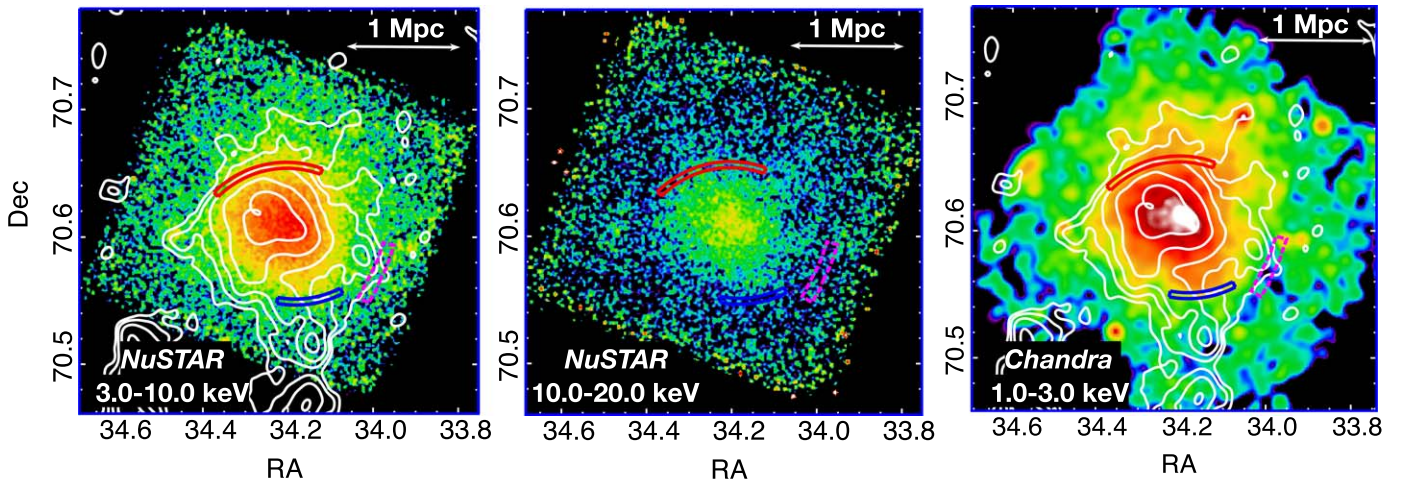
Throughout this paper, we assume Lambda cold dark matter ( $\Lambda$ CDM) cosmology with  $H_0 = 70 \text{ km s}^{-1} \text{ Mpc}^{-1}$ ,  $\Omega_M = 0.3$ , and  $\Omega_\Lambda = 0.7$ . According to these assumptions, at the cluster redshift ( $z = 0.18$ ), a projected intracluster distance of 100 kpc corresponds to an angular separation of  $\sim 32''$ . All uncertainties are quoted at 68% confidence levels unless otherwise stated.

## 2. Observations and Data Reduction

### 2.1. NuSTAR

In this work, we use NuSTAR (Harrison et al. 2013) observations of CL 0217+70 with Observation IDs 70701001002 and 70701001004 using both focal plane modules, namely, FPMA and FPMB. The specifications of the data used in our analysis are summarized in Table 1.

In order to filter the data, standard pipeline processing using HEASoft (v. 6.28) and NuSTARDAS (v. 2.0.0) tools are used. To clean the event files, stages 1 and 2 of the NuSTARDAS pipeline processing script `nupipeline` are used. Regarding the cleaning of the event files for the passages through the South Atlantic Anomaly (SAA) and a “tentacle”-like region of higher activity near part of the SAA, instead of using `SAAMODE = STRICT` and `TENTACLE = yes` calls, we



**Figure 1.** Background-subtracted, exposure-corrected photon images of CL 0217+70 in the 3.0–10.0 keV NuSTAR (left panel), 10.0–20.0 keV NuSTAR (middle panel), and 1.0–3.0 keV Chandra (right panel) bands. LOFAR contour levels (white) correspond to  $\sigma_{\text{rms}} \times [3, 6, 12, 24, 48]$  ( $\sigma_{\text{rms}} = 330 \mu\text{Jy beam}^{-1}$  [ $46'' \times 45''$ ]) (Hoang et al. 2021). Red and blue arcs correspond to the location of northern and southern SB edges proposed by Zhang et al. (2020b), respectively. The channel region is indicated with a dashed magenta rectangle.

have created light curves and applied different filters to create good time intervals (GTIs) manually without fully discarding the passage intervals.

The new set of GTIs are reprocessed with `nupipeline` stages 1 and 2, and images are generated at different energy bands with XSELECT. To create exposure maps, `nuexpomap` is used. To produce the corresponding spectra for the regions of interest as well as the corresponding Response Matrix Files (RMFs) and Ancillary Response Files (ARFs), stage 3 of the `nuproducts` pipeline are used.

The main components of the NuSTAR background are instrument Compton scattered continuum emission, instrument activation and emission lines, cosmic X-ray background from the sky leaking past the aperture stops, reflected solar X-rays, and focused and ghost-ray cosmic X-ray background. Modeling the background where there is a lack of cluster emission regions is not straightforward since the ICM emission becomes an additional component in the background fitting procedure. To apply these models for the cluster background assessment, a set of IDL routines called `nuskybgd` (Wik et al. 2014), which defines the background spatially and spectrally, is utilized.

The procedure starts with selecting regions in the field of view (FOV) where the cluster emission is inherently present yet not the most dominant. To account for the ICM emission, a single-temperature `apec` model is included in the full set of models, and jointly fitted with the background components. The point sources detected in the Chandra FOV were not originally excluded from these regions, since they did not become apparent until after the background subtraction. While they may bias the focused cosmic X-ray background (fCXB) component in some regions, the average fCXB level is used to produce background spectra in all regions, lessening their impact, which is already only  $\sim 10\%$  of the total background. We discuss the systematics in Appendix A.

The global background model is then used to create background images, which are then subtracted from the images and are corrected by the corresponding exposure maps. Background-subtracted, exposure-corrected images at different energy bands are presented in the left and middle panels of Figure 1. Region selection and the background fits are presented in Appendix A.

Once the background is defined for any region in the FOV both spatially and spectrally, the next step is to select regions of interest, to extract spectra and the corresponding files and generate the specific background model, followed by spectral fitting to evaluate the physical properties of the ICM.

## 2.2. Chandra

We use the observation and blank-sky background event files obtained from the 25 ks Chandra archival data (Observation ID: 16293) produced by Zhang et al. (2020b) for the data analysis. We use the Chandra Interactive Analysis of Observations (CIAO) v4.12 package with CALDB 4.9.0 for extracting the spectra. Background-subtracted, exposure-corrected image in the 1.0–3.0 keV band are presented in the right panel of Figure 1.

In addition to NuSTAR and Chandra data, we also represent the Low-Frequency Array (LOFAR) data, courtesy of Hoang et al. (2021, Figure 4 therein). The LOFAR image of the cluster showing the relics and the central region is presented in Figure 2.

## 3. Data Analysis and Results

### 3.1. Global Properties

We began our analysis with the assessment of the global properties of the cluster. We selected a circular region centered at the X-ray emission peak with  $r = 5/2$  ( $\sim 1$  Mpc), following the extent of the radio halo emission. We extracted a spectrum from NuSTAR, which then was fit by a single-temperature `apec` model (Smith et al. 2001), i.e.,  $\text{constant} \times \text{apec}$ , i.e., 1T model, with XSPEC (v. 12.11.1).

The redshift value of the cluster is freed to vary due to the gain issue of NuSTAR (R. A. Rojas Bolivar et al., submitted). Once the best-fit values are found for the redshift, we then freeze these parameters during error calculations. We apply the maximum likelihood-based statistic (hereafter, C-stat) appropriate for Poisson data as proposed by Cash (1979). Photon counts used in spectral analysis are grouped to have at least three counts in each bin.

We then applied this method to the joint analysis of NuSTAR and Chandra data. For all of the joint analyses, we



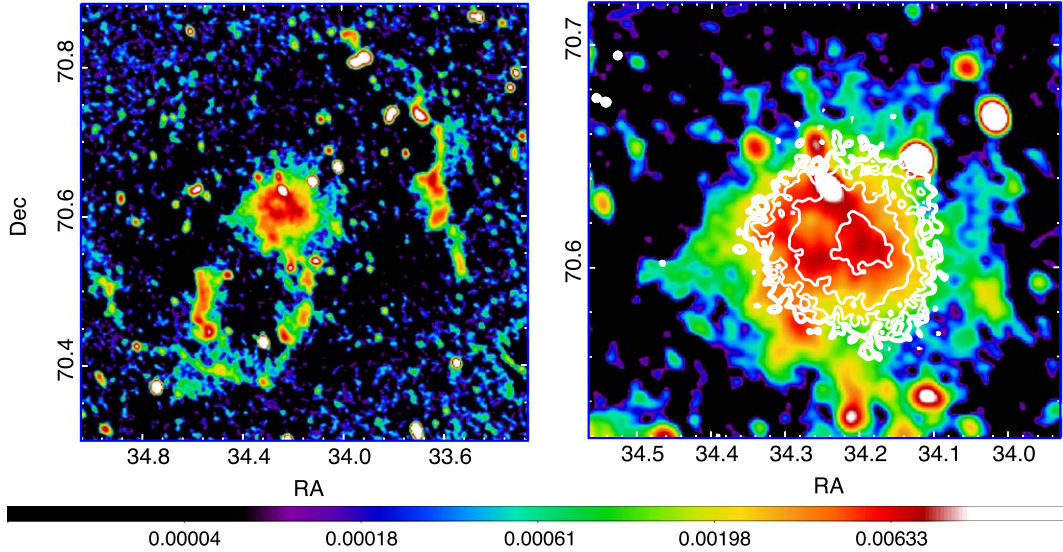


Figure 2. LOFAR  $26''6 \times 22''5$  resolution image (Hoang et al. 2021) with 3.0–10.0 keV NuSTAR contours overlaid.

convolve the model with `TBabs` since Chandra is susceptible to  $N_H$ , and we let this parameter free. CL 0217+70 lies within  $9^\circ$  of the Galactic plane and consequently suffers from a high foreground column density ( $N_H \sim 8 \times 10^{21} \text{ cm}^{-2}$ ), which absorbs most X-ray photons with energies below a few keV. Near the plane, it is also expected that the column density will be variable on arcminute scales, which cannot be reliably predicted from atomic hydrogen (HI) estimates. Due to NuSTAR’s lack of bandpass sensitivity below 3 keV, we are able to ignore foreground absorption at this level (Rojas Bolivar et al. 2021) for NuSTAR analysis for simplicity. However, we report  $\sim 0.2$  keV difference with/without the inclusion of an absorption model with  $N_H \sim 8 \times 10^{21} \text{ cm}^{-2}$  for the global fit. However, when the  $N_H$  parameter is freed to vary, the face value becomes  $10^{17} \text{ cm}^{-2}$ , where the lower limit hits the hard limit of zero and with the higher limit reaching on to  $10^{19} \text{ cm}^{-2}$ . This unphysical behavior of the parameter points to NuSTAR’s lack of sensitivity to  $N_H$  at low energies.

The spectral fit results of the parameters are presented in Table 2 and Table 3 for NuSTAR and for joint NuSTAR and Chandra, respectively. To study the nonisothermal gas expected from merging clusters of galaxies, as well as possible nonthermal emission due to IC scattering, we applied two more models to the spectra following the work of Rojas Bolivar et al. (2021) and Wik et al. (2014).

We first added another `appec` component to the 1T model to describe a secondary temperature structure, and fitted the spectra with `constant × (appec + appec)`, namely the 2T model. We then used another model 1T+IC : `constant × (appec + powerlaw)`, accounting for the thermal emission and a possible IC emission, where the IC component is represented with a power-law distribution. We fixed the photon index to  $\Gamma = 2$  of the power law obtained from the spectral index found by Hoang et al. (2021).

The addition of a second `appec` and a power law to the original single-temperature model for NuSTAR spectrum resulted in an improvement of  $\Delta C/\Delta \nu = 41.25/2$  and  $\Delta C/\Delta \nu = 38.30/1$  for the 2T and 1T + IC model, respectively, with respect to single-temperature fit. For the joint

**Table 2**  
Spectral Parameters and  $1\sigma$  Uncertainty Ranges of NuSTAR Global Spectrum Fits in 3.0–20.0 band for 1T: `constant × appec`, 2T: `constant × (appec + appec)`, and 1T + IC: `constant × (appec + powerlaw)`

	1T	2T	1T + IC
$kT_1$ (keV)	$9.13 \pm 0.12$	$10.60^{+0.79}_{-0.44}$	$7.76^{+0.26}_{-0.25}$
$Z_1$ ( $Z_\odot$ )	$0.198 \pm 0.026$	$0.280^{+0.034}_{-0.032}$	$0.282^{+0.036}_{-0.034}$
$z_1$	0.222	0.222	0.219
$\text{norm}_1$ ( $10^{-2}$ )	$1.369 \pm 0.018$	$1.139^{+0.060}_{-0.073}$	$1.045^{+0.049}_{-0.046}$
$kT_2$	...	$2.16^{+1.14}_{-0.52}$	...
$\text{norm}_2$ ( $10^{-2}$ )	...	$0.728^{+0.312}_{-0.156}$	...
$\Gamma$	...	...	2.0 (fixed)
$\kappa$ ( $10^{-2}$ )	...	...	$0.121^{+0.016}_{-0.018}$
$C/\nu$	1679.29/1686	1638.04/1684	1640.99/1685

**Note.** For the 2T model, abundance and redshift values of two `appec` components are tied to each other within instruments. `appec` normalization ( $n$ ) is given in  $\frac{10^{-14}}{4\pi[D_A(1+z)]^2} \int n_e n_H dV$  where power-law normalization ( $\kappa$ ) is photons  $\text{keV}^{-1} \text{ cm}^{-2} \text{ s}^{-1}$  at 1 keV.

NuSTAR and Chandra analysis, the fit also improved by an additional `appec` or a power-law component, where we found  $\Delta C/\Delta \nu = 36.96/2$  and  $\Delta C/\Delta \nu = 32.30/1$  for 2T and 1T + IC, respectively. Both NuSTAR and joint NuSTAR and Chandra analysis show that the central  $r = 5''.2$  emission is best described by the 2T model.

We also calculated the luminosity of the cluster from the NuSTAR spectra within this region ( $r = 31''.2 \simeq 0.6 r_{500}$ , adopting  $r_{500} = 500''$ ; Reiprich et al. 2013). We find the X-ray bolometric (0.01–100 keV) luminosity to be  $L_{X,\text{bol}} = 1.390 \times 10^{45} \text{ erg s}^{-1}$ , and within 0.5–2.0 keV we find  $L_{X,0.5-2.0\text{keV}} = 2.716 \times 10^{43} \text{ erg s}^{-1}$  using the XSPEC convolution model `clumin`, for the 1T model.

The NuSTAR gain issue is usually accommodated for by the use of the `xspec gain` command. The gain over the years has shown an offset value around  $-0.1$ , but is still a work under construction (Rojas Bolivar et al., submitted). In the global

**Table 3**  
Same as Table 2 but for Joint NuSTAR (3.0–20.0 keV) and Chandra (0.8–7.0 keV) Global Spectral Fit

	1T	2T	1T + IC
$N_H$ ( $10^{21}$ cm $^{-2}$ )	$9.17 \pm 0.25$	$9.80 \pm 0.27$	$10.06 \pm 0.33$
$kT_1$ (keV)	$9.20^{+0.11}_{-0.12}$	$21.56^{+2.71}_{-2.90}$	$7.99^{+0.25}_{-0.24}$
$Z_{IN}$ ( $Z_\odot$ )	$0.202 \pm 0.026$	$0.214 \pm 0.024$	$0.273^{+0.034}_{-0.033}$
$Z_{IC}$ ( $Z_\odot$ )	$0.550^{+0.110}_{-0.105}$	$0.572^{+0.102}_{-0.097}$	$0.750^{+0.135}_{-0.128}$
$z_{IN}$	0.228	0.219	0.221
$z_{IC}$	0.188	0.185	0.186
norm $_1$ ( $10^{-2}$ )	$1.376 \pm 0.017$	$0.364^{+0.095}_{-0.062}$	$1.081^{+0.048}_{-0.047}$
$kT_2$	...	$6.36^{+0.40}_{-0.38}$	...
norm $_2$ ( $10^{-2}$ )	...	$1.133^{+0.061}_{-0.096}$	...
$\Gamma$	...	...	2.0 (fixed)
$\kappa$ ( $10^{-2}$ )	...	...	$0.107^{+0.018}_{-0.016}$
$C/\nu$	2104.29/2107	2067.33/2105	2071.99/2106

**Note.** All models are convolved with TBabs. During the error calculations, redshifts ( $z$ ) are fixed to the best-fit values. Subscripts “N” refer to NuSTAR and “C” refer to Chandra parameters.

spectral analysis using the 1T model, we found that the gain is  $-0.15$ . When we use the `gain` command, the temperature becomes  $kT = 9.15^{+0.17}_{-0.12}$  keV with 1684.29/1685 d.o.f., and the temperature is  $kT = 9.13 \pm 0.12$  keV with 1679.29/1686 d.o.f., when the redshift is freed to vary. Using the `gain` command instead of freeing the redshift changes the temperature by only 0.3%, but does not necessarily provide a better model. Due to the complexity of applying the `gain` command further in our analyses, we chose to free the redshift to account for the gain issue for the rest of this work.

In addition, here we share the luminosities that account for the evolution of the  $L_X$ - $T$  scaling relations, using  $E(z) = 1.09$ , where  $E(z) = \sqrt{\Omega_M(1+z)^3 + (1 - \Omega_M - \Omega_\Lambda)(1+z)^2 + \Omega_\Lambda}$  (Giles et al. 2016). Dividing the obtained luminosities by  $E(z)$ , the luminosity values become  $L_{X,\text{bol}} = 1.275 \times 10^{45}$  erg s $^{-1}$  and  $L_{X,0.5-2.0\text{keV}} = 2.492 \times 10^{43}$  erg s $^{-1}$ .

The resulting spectra are shown in Appendix B.

### 3.2. Surface Brightness Discontinuities

To study the correspondences of northern and southern Chandra SB edges (Figure 1) with NuSTAR, we used a Gaussian gradient magnitude (GGM) filter<sup>14</sup> (Sanders et al. 2016). Assuming Gaussian derivatives with a width of  $\sigma$ , the GGM filter calculates the gradient of an image. To create the GGM-filtered image, the image itself is convolved by the gradient of a 1D Gaussian function for two axes, then these two resulting images are combined for the 2D gradient image. The width,  $\sigma$ , is varied to capture gradients on different scales, i.e., small  $\sigma$  values are used at the central regions where there are many counts, and high values better capture the gradient at cluster outskirts with low counts.

Since NuSTAR’s point-spread function (PSF) is much larger than the Chandra PSF for which the GGM filter was intended for, the filters with low levels of sigma ( $\sigma = 1, 2$ ) were mainly dominated by noise. Therefore, we present the GGM filtered to the background-subtracted, exposure-corrected images using  $\sigma = 4, 8$ , and 16 detector pixels, as shown in Figure 3.

Due to the large PSF of NuSTAR, the northern and southern SB edges are not unambiguously visible from the GGM results. We note that the SB edge and the channel locations obtained from Zhang et al. (2020b) are overlaid on the GGM (Figure 3) merely to guide the eye and are not indicated by GGM analysis. The use of the GGM in this context is to reveal the strong SB feature much closer to the cluster center than the Chandra-detected northern and southern SB edges.

The GGM points to a sharp gradient best discerned in the panels presenting the  $\sigma = 8, 3.0$ – $10.0$ , and  $3.0$ – $30.0$  keV bands and the  $\sigma = 16, 3.0$ – $10.0$  keV band, suggesting a SB edge. This edge can also be seen in NuSTAR, Chandra, and LOFAR images. For a better visualization of this edge, we present the NuSTAR GGM, NuSTAR photon, Chandra photon, and LOFAR images together in Figure 4.

### 3.3. Temperature Map

To study the temperature structure of the NuSTAR FOV, we created a temperature map. We extracted count images from a  $12' \times 12'$  central box region of the cluster in the 3.0–5.0, 6.0–10.0, and 10.0–20.0 keV bands where the point sources detected by Chandra were excluded. We avoided the 5.0–6.0 keV band due to the existence of the FeK complex. The background images and exposure maps were extracted for the same energy bands with `nuskybgd` and `nuproducts`, respectively.

The background-subtracted, exposure-corrected images were then used for the spectral extraction, and predefined pixels were fitted with a single-temperature `apec` model, during which the abundance and redshift were fixed to the values obtained from the global fit. The technique is described in detail by Markevitch et al. (2000). The resulting temperature map is presented in Figure 5. We emphasize that this temperature map is a very basic analysis tool to search for any strong features in the ICM as in the case of the GGM analysis. We present more quantitative, accurate, and precise temperature results further in this work.

In the temperature map, we encountered a “hot spot”<sup>15</sup> that has a higher temperature than the cluster core. In the vicinity ( $\sim 0.5$ ) of the “hot spot” (Figure 5, turquoise circle), there is a radio source GB3 0212+704<sup>16</sup> (Figure 5, blue circle) (Maslowski 1972) and LOFAR high-resolution study shows a tail morphology. The spectral index map between LOFAR 145 MHz and VLA 1.5 GHz also shows the steepening of the spectrum behind the tail. The tail radio galaxy has a flux density of  $S$  (141 MHz) =  $12.1 \pm 1.2$  mJy,  $S$  (1.4 GHz) =  $2.9 \pm 0.2$  mJy,  $S$  (1.5 GHz) =  $2.7 \pm 0.2$  mJy. The average spectral index is  $\alpha = -0.62 \pm 0.01$ .

To study this feature in detail with NuSTAR, we extracted a circular region with  $r = 0.6$  ( $\sim 112$  kpc) enclosing the most dominant region of this “hot spot”, centered at 2:17:04.08 (R. A.) and +70:39:06 (decl.). The temperature map indicates that, if of thermal origin, the temperature of the plasma is  $\geq 12$  keV. This feature may be a part of a more extended emission, yet it is difficult to define this extension.

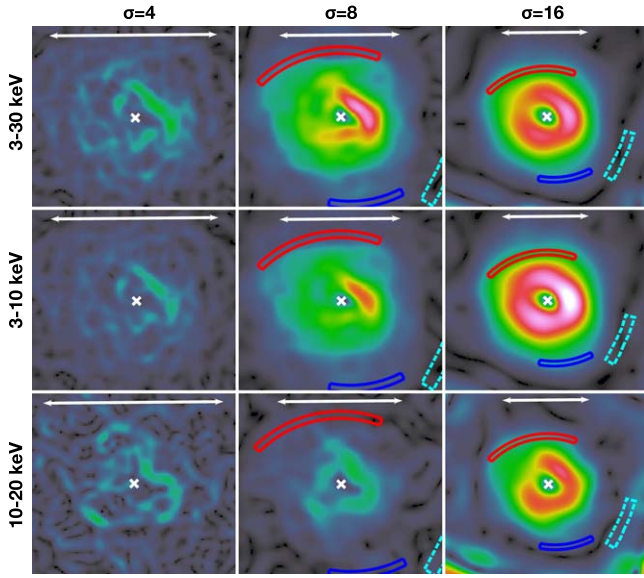
To explain its nature, we put forward three scenarios. Scenario 1 suggests that the feature is the downstream shock

<sup>15</sup> “Hot spot” refers to the feature of unknown origin seen in the temperature map, while without quotations we refer to a thermal plasma emission.

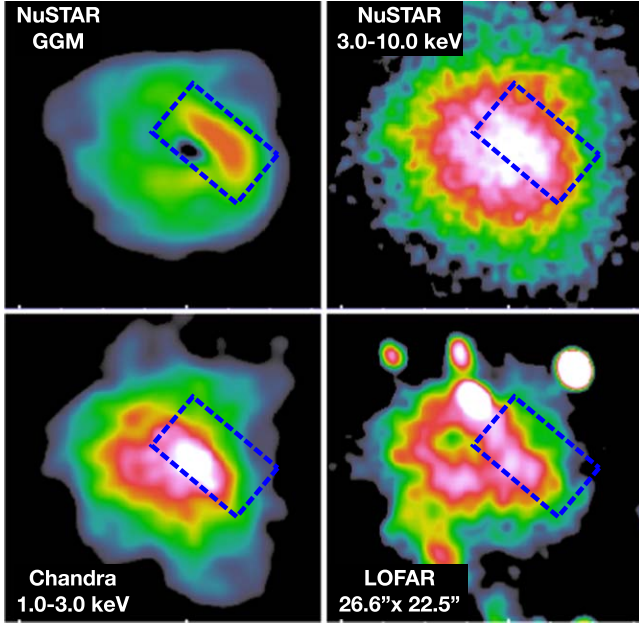
<sup>16</sup> <https://vizier.cds.unistra.fr/viz-bin/VizieR-5?-ref=VIZ620b3ce430f570&-out.add=&-source=VIII/53/gb1&rcno=3648>

<sup>14</sup> <https://github.com/jeremysanders/ggm>





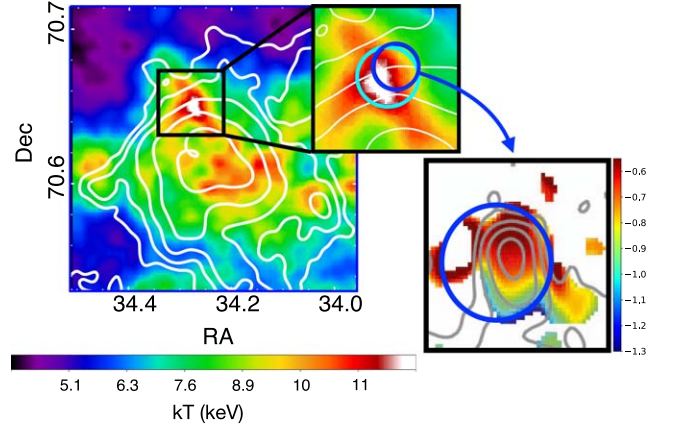
**Figure 3.** NuSTAR GGM-filtered background-subtracted, exposure-corrected images in the 3.0–30.0 keV (top panels), 3.0–10.0 keV (middle horizontal panels), and 10.0–20.0 keV (lower panels) energy bands. White crosses correspond to the emission peaks, red (blue) arcs correspond to the northern (southern) SB edges, and dashed turquoise regions represent the channel. The white arrows in each image correspond to 1 Mpc.



**Figure 4.**  $\sigma = 8$ , 3.0–10.0 keV NuSTAR GGM (upper left), NuSTAR 3.0–10.0 keV photon (upper right), Chandra 1.0–3.0 keV photon (lower left), and LOFAR  $26.6'' \times 22.5''$  resolution (lower right) images. The dashed blue boxes correspond to the same region in all images.

region, evidenced by its location on the northern Chandra SB edge. Scenario 2 is an emission from a heavily obscured AGN (since Chandra does not detect it) that may be due to a strong chaotic cold accretion (CCA) rain that feeds the central supermassive black hole (Gaspari et al. 2013, 2020). Scenario 3 is a localized IC emission where the electrons in the nearby radio source are upscattered to the X-ray regime by a possible shock front.

We first fit the NuSTAR spectra with a single-temperature  $apec$  model (Scenario 1). The temperature obtained from this



**Figure 5.** NuSTAR temperature map with radio contours from LOFAR (white, at  $\sigma_{\text{rms}} \times [3, 6, 12, 24, 48]$ , where  $\sigma_{\text{rms}} = 330 \mu\text{Jy beam}^{-1}$  [ $46'' \times 45''$ ]) are overlaid. In the zoomed-in panel (black box, upper-right corner), the “hot spot” is indicated by a turquoise circle, and the radio source is shown with a blue circle. In the lower-right corner, the radio galaxy spectral map between 141 MHz (LOFAR) and 1.5 GHz (VLA) at  $16''$  resolution is shown (Hoang et al. 2021, Figure 6 therein).

**Table 4**

Spectral Parameters and  $1\sigma$  Uncertainty Ranges of NuSTAR Spectrum Fits in 3.0–20.0 keV Band of the “Hot Spot” Scenarios

	Hot spot	Obscured AGN	IC
$N_H$ ( $10^{22} \text{ cm}^{-2}$ )	...	$5.11^{+3.63}_{-3.52}$	...
$kT$ (keV)	$12.10^{+2.01}_{-1.29}$	...	...
$Z$ ( $Z_\odot$ )	$0.612^{+0.388}_{-0.312}$	...	...
$z$	$0.249^{+0.046}_{-0.033}$	...	...
norm ( $10^{-4}$ )	$1.497^{+0.187}_{-0.158}$	...	...
$\Gamma$	...	$2.34^{+0.18}_{-0.17}$	$2.13^{+0.09}_{-0.08}$
$\kappa$ ( $10^{-4}$ )	...	$1.100^{+0.542}_{-0.356}$	$0.657^{+0.120}_{-0.102}$
$C/\nu$	381.91/364	382.37/365	384.50/366

fit was  $kT = 12.1^{+2.0}_{-1.3}$  keV with  $C/\nu = 381.91/364$ . To test Scenario 2, we used a power-law model convolved with a  $\text{TBabs}$  model to account for a heavily obscured AGN. The resulting hydrogen column density value is  $N_H = 5.11 \times 10^{22} \text{ cm}^{-2}$ , where the photon index for the hypothesized AGN emission is  $\Gamma = 2.34^{+0.18}_{-0.17}$ . The statistics of this fit is  $C/\nu = 382.37/365$ . And for Scenario 3, we used an unabsorbed power-law model to describe possible IC emission. The resulting power-law slope is  $\Gamma = 2.13^{+0.09}_{-0.08}$ . The statistics of this fit is  $C/\nu = 384.50/366$ . The corresponding values and spectra of the fits from these scenarios are presented in Table 4 and in Appendix C, respectively. Statistics show that these three scenarios are equally likely.

Lastly, to rule out a possible multi-temperature structure, we also fitted a two-temperature model to the spectrum. The high-temperature component rose up to  $kT \sim 28.8$  keV, where the low-temperature component was  $kT \sim 7.41$ . In this fit, both temperature parameters were unconstrained.

### 3.4. Cross-talk Analysis

Even single bright sources in the NuSTAR FOV cause scattered photons due to the large ( $\sim 1'$  half-power diameter,  $\sim 18''$  FWHM), slightly energy-dependent PSF. This results in a cross-contamination, namely cross-talk, of multiple emission sources in the regions of interest, although the emission may

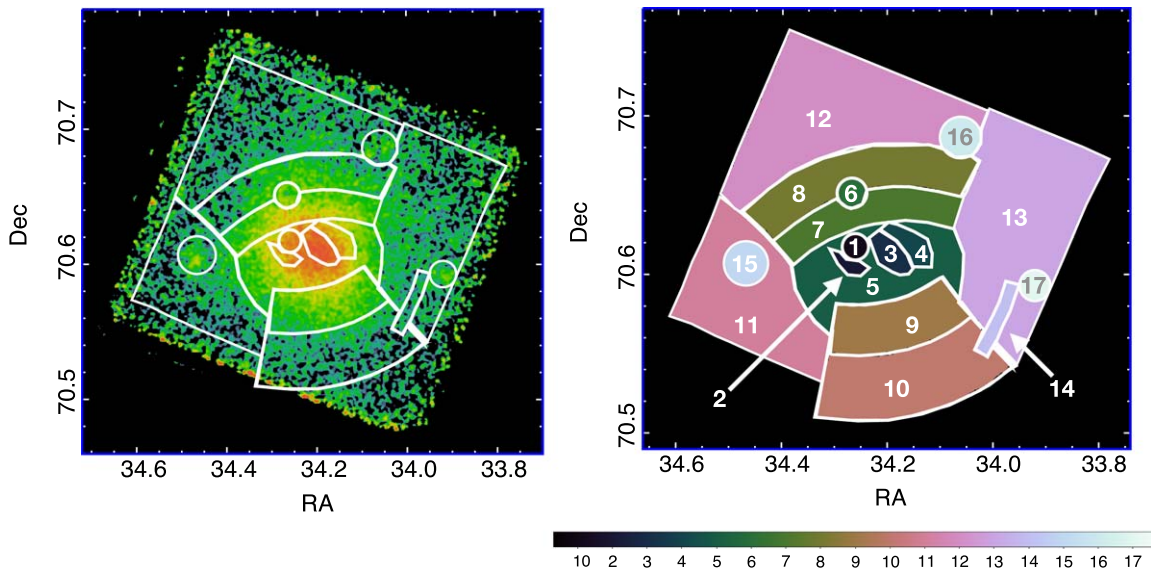


Figure 6. Regions selected for the cross-talk assessment.

not originate from the selected region. `nuproducts` produces ARFs for point or diffuse sources inside the user-defined extraction regions. However, it does not account for the ARFs for other sources whose emission originates outside these extraction regions that contaminate the spectra of those regions. These ARFs will be referred to as cross-ARFs.

The software, composed of a set of routines created to account for this contamination, is `nucrossarf`.<sup>17</sup>

In order to study the temperature jumps and prominent structures in the FOV more accurately, we selected regions of interest in the NuSTAR data and used `nucrossarf` to account for the cross-talk. The selected regions are overlaid on the NuSTAR image on the left panel, and the corresponding region values are presented in the right panel of Figure 6.

The motivation behind selecting regions are based on the recent Chandra study proposing SB edges, the results of our NuSTAR GGM and temperature map results, and LOFAR images. Region 1 corresponds to the radio SB depression as seen in the LOFAR image (Figure 2, right panel). Region 2 is a wedge, again evidenced by LOFAR image. We selected these regions to investigate any correspondence of these radio features with the X-ray data. Regions 3 ( $C_{in}$ ) and 4 ( $C_{out}$ ) correspond to the inner and outer side of the central SB edge, respectively, as highlighted in Figure 4. Region 5 represents the central region of the cluster that excludes the emission from Regions 1, 2, 3, and 4. Region 6 is the “hot spot,” which we investigate with the aforementioned three scenarios in Section 3.3.

Regions 7 ( $N_{in}$ ) and 8 ( $N_{out}$ ) are the inner (downstream) and outer (upstream) part of the northern SB edge proposed by Zhang et al. (2020b), respectively, and, similarly, Regions 9 ( $S_{in}$ ) and 10 ( $S_{out}$ ) are the inner and outer sides of the southern SB, respectively. We note that Regions 7, 8, 9 and 10 are not the exact regions selected by Zhang et al. (2020b) that were used to draw the SB profiles on the corresponding edges in their work. The NuSTAR FOV ( $13' \times 13'$ ) is considerably smaller than the Chandra FOV ( $16' \times 16'$ ), and the regions they use for the SB profiles exceeds our FOV. We widened the angle of the southern and northern edge arcs to be able to

capture as many upstream photons as possible for better statistics.

Regions 11, 12, and 13 indicate the outer cluster emission at different directions that is most likely isothermal. The channel is represented by Region 14. Finally, Regions 15, 16, and 17 are point sources as seen by Chandra and NuSTAR.

We extracted spectra from these 17 regions in total using `nuproducts`, and found the best-fit model for these regions. In total, we have 13 regions to account for the ICM emission modeled by an `apec`, and three point sources (circular regions in Figure 6) modeled by a power law. And for Region 6, we use three different models, as explained in detail in Section 3.3.

During the `nucrossarf` fit, we fitted 17 spectra and their individual 17 ARFs simultaneously, where we fixed the redshift and abundance values to the individual `nuproducts` spectral fits. For Region 6, we studied the three scenarios. We ran the `nucrossarf` code thrice, first treating Region 6 as a hot spot, then an obscured AGN, and, finally, localized IC emission. The results from the `nuproducts` and `nucrossarf` spectral analysis are given in Table 5.

We note that Region 14, where Chandra detects the possible SB depression (Channel), the upper limits for  $kT$  and `apec` normalization were quite large, therefore we constrained the upper limits to 9 keV and  $1 \times 10^{-3} \text{ cm}^{-5}$  for the temperature and `apec` normalization, respectively.

For all of the AGN power-law models, we fixed the photon index to the `nuproducts` value to prevent an artificial gauge of any excess in the hard band regime by the power-law model. Since these regions are treated as point sources and since the regions attributed to them are comparable to the NuSTAR PSF, their emission should be localized, meaning the shape of the slope would be conserved.

To better visualise the effect of the inclusion of cross-talk analysis, we present temperature maps created by filling the regions of interest with the obtained temperature values from the fits in Figure 7. This figure, showing the temperature results from all scenarios, is also a testament to the stability of the cross-talk analysis, as they visualize the almost-identical temperature values when we assume difference emission models for Region 6.

<sup>17</sup> <https://github.com/danielrwik/nucrossarf>



**Table 5**  
Cross-talk Analysis Spectral Fit Results where Region 6 is Treated as a Hot Spot, Obscured AGN, and Inverse Compton Emission

Region Number	$kt$ (keV) or $\Gamma$				norm or $\kappa$				Notes
	nuproducts	nucrossarf			nuproducts	nucrossarf			
		Hot Spot	AGN	IC		Hot Spot	AGN	IC	
1	10.18 <sup>+0.68</sup> <sub>-0.33</sub>	9.90 <sup>+1.90</sup> <sub>-1.38</sub>	9.89 <sup>+1.90</sup> <sub>-1.38</sub>	9.90 <sup>+1.90</sup> <sub>-1.38</sub>	0.356 <sup>+0.023</sup> <sub>-0.021</sub>	0.459 <sup>+0.056</sup> <sub>-0.051</sub>	0.460 <sup>+0.060</sup> <sub>-0.051</sub>	0.459 <sup>+0.056</sup> <sub>-0.051</sub>	
2	9.47 <sup>+0.62</sup> <sub>-0.73</sub>	7.47 <sup>+2.44</sup> <sub>-1.88</sub>	7.48 <sup>+2.46</sup> <sub>-1.87</sub>	7.43 <sup>+2.45</sup> <sub>-1.85</sub>	0.235 <sup>+0.018</sup> <sub>-0.019</sub>	0.217 <sup>+0.061</sup> <sub>-0.042</sub>	0.218 <sup>+0.060</sup> <sub>-0.042</sub>	0.219 <sup>+0.061</sup> <sub>-0.042</sub>	
3	11.18 <sup>+0.43</sup> <sub>-0.20</sub>	12.53 <sup>+0.94</sup> <sub>-0.83</sub>	12.55 <sup>+0.95</sup> <sub>-0.82</sub>	12.51 <sup>+0.94</sup> <sub>-0.83</sub>	0.996 <sup>+0.038</sup> <sub>-0.034</sub>	1.406 <sup>+0.060</sup> <sub>-0.048</sub>	1.409 <sup>+0.060</sup> <sub>-0.048</sub>	1.407 <sup>+0.061</sup> <sub>-0.049</sub>	C <sub>in</sub>
4	10.61 <sup>+0.49</sup> <sub>-0.46</sub>	10.29 <sup>+0.93</sup> <sub>-0.71</sub>	10.25 <sup>+0.91</sup> <sub>-0.71</sub>	10.31 <sup>+0.92</sup> <sub>-0.71</sub>	0.573 <sup>+0.030</sup> <sub>-0.028</sub>	0.800 <sup>+0.041</sup> <sub>-0.042</sub>	0.801 ± 0.041	0.799 <sup>+0.041</sup> <sub>-0.042</sub>	C <sub>out</sub>
5	9.92 <sup>+0.16</sup> <sub>-0.22</sub>	9.37 <sup>+0.42</sup> <sub>-0.44</sub>	9.35 <sup>+0.42</sup> <sub>-0.45</sub>	9.40 <sup>+0.42</sup> <sub>-0.44</sub>	3.452 <sup>+0.089</sup> <sub>-0.063</sub>	3.626 <sup>+0.134</sup> <sub>-0.123</sub>	3.635 <sup>+0.139</sup> <sub>-0.124</sub>	3.617 <sup>+0.134</sup> <sub>-0.121</sub>	
6	12.02 <sup>+1.76</sup> <sub>-1.31</sub>	21.02 <sup>a</sup>	...	...	0.149 <sup>+0.017</sup> <sub>-0.016</sub>	0.108 ± 0.012	...	...	Hot spot
6	2.34 <sup>+0.18</sup> <sub>-0.17</sub>	...	2.34 <sup>b</sup>	...	0.110 <sup>+0.054</sup> <sub>-0.036</sub>	...	0.054 ± 0.007	...	AGN
6	2.13 <sup>+0.09</sup> <sub>-0.08</sub>	...	...	1.38 ± 0.26	0.066 <sup>+0.012</sup> <sub>-0.010</sub>	...	...	0.014 <sup>+0.010</sup> <sub>-0.006</sub>	IC
7	9.29 <sup>+0.27</sup> <sub>-0.16</sub>	8.31 <sup>+0.43</sup> <sub>-0.41</sub>	8.57 <sup>+0.45</sup> <sub>-0.41</sub>	8.12 <sup>+0.44</sup> <sub>-0.40</sub>	1.862 <sup>+0.051</sup> <sub>-0.027</sub>	2.028 <sup>+0.088</sup> <sub>-0.082</sub>	2.014 <sup>+0.084</sup> <sub>-0.081</sub>	2.067 <sup>+0.094</sup> <sub>-0.089</sub>	N <sub>in</sub>
8	7.51 <sup>+0.30</sup> <sub>-0.53</sub>	6.70 <sup>+0.52</sup> <sub>-0.47</sub>	6.98 <sup>+0.54</sup> <sub>-0.49</sub>	6.56 <sup>+0.51</sup> <sub>-0.47</sub>	1.449 <sup>+0.055</sup> <sub>-0.114</sub>	1.342 <sup>+0.098</sup> <sub>-0.090</sub>	1.319 <sup>+0.093</sup> <sub>-0.086</sub>	1.374 <sup>+0.105</sup> <sub>-0.095</sub>	N <sub>out</sub>
9	8.98 <sup>+0.39</sup> <sub>-0.31</sub>	8.19 <sup>+0.45</sup> <sub>-0.44</sub>	8.20 <sup>+0.45</sup> <sub>-0.43</sub>	8.18 <sup>+0.45</sup> <sub>-0.43</sub>	1.527 <sup>+0.061</sup> <sub>-0.053</sub>	1.575 <sup>+0.072</sup> <sub>-0.064</sub>	1.578 <sup>+0.072</sup> <sub>-0.064</sub>	1.577 <sup>+0.072</sup> <sub>-0.065</sub>	S <sub>in</sub>
10	8.05 <sup>+0.72</sup> <sub>-0.59</sub>	6.02 <sup>+0.97</sup> <sub>-0.72</sub>	6.02 <sup>+0.97</sup> <sub>-0.72</sub>	6.02 <sup>+0.98</sup> <sub>-0.72</sub>	0.819 <sup>+0.055</sup> <sub>-0.054</sub>	0.645 <sup>+0.090</sup> <sub>-0.082</sub>	0.646 <sup>+0.090</sup> <sub>-0.082</sub>	0.645 <sup>+0.090</sup> <sub>-0.082</sub>	S <sub>out</sub>
11	7.13 <sup>+0.54</sup> <sub>-0.42</sub>	4.46 <sup>+0.57</sup> <sub>-0.62</sub>	4.44 <sup>+0.56</sup> <sub>-0.63</sub>	4.40 <sup>+0.57</sup> <sub>-0.61</sub>	1.195 <sup>+0.075</sup> <sub>-0.071</sub>	0.956 <sup>+0.177</sup> <sub>-0.112</sub>	0.960 <sup>+0.181</sup> <sub>-0.120</sub>	0.953 <sup>+0.175</sup> <sub>-0.119</sub>	
12	4.72 <sup>+0.29</sup> <sub>-0.37</sub>	3.16 <sup>+0.22</sup> <sub>-0.20</sub>	3.15 <sup>+0.22</sup> <sub>-0.20</sub>	3.18 <sup>+0.23</sup> <sub>-0.21</sub>	2.921 <sup>+0.226</sup> <sub>-0.206</sub>	3.765 <sup>+0.427</sup> <sub>-0.380</sub>	3.803 <sup>+0.426</sup> <sub>-0.385</sub>	3.740 <sup>+0.427</sup> <sub>-0.379</sub>	
13	9.97 <sup>+0.82</sup> <sub>-0.52</sub>	7.40 <sup>+0.64</sup> <sub>-0.60</sub>	7.37 <sup>+0.63</sup> <sub>-0.61</sub>	7.42 <sup>+0.65</sup> <sub>-0.60</sub>	1.819 <sup>+0.104</sup> <sub>-0.077</sub>	1.667 <sup>+0.112</sup> <sub>-0.107</sub>	1.672 <sup>+0.123</sup> <sub>-0.107</sub>	1.664 <sup>+0.112</sup> <sub>-0.107</sub>	
14	8.25 <sup>+2.26</sup> <sub>-1.94</sub>	2.17 <sup>+.....</sup> <sub>-1.29</sub> <sup>c</sup>	2.20 <sup>+.....</sup> <sub>-1.31</sub> <sup>c</sup>	2.17 <sup>+.....</sup> <sub>-1.29</sub> <sup>c</sup>	0.052 <sup>+0.013</sup> <sub>-0.013</sub>	0.140 <sup>+.....</sup> <sub>-0.130</sub> <sup>d</sup>	0.138 <sup>+.....</sup> <sub>-0.128</sub> <sup>d</sup>	0.141 <sup>+.....</sup> <sub>-0.131</sub> <sup>d</sup>	Channel
15	2.17 ± 0.13	2.17 <sup>b</sup>	2.17 <sup>b</sup>	2.17 <sup>b</sup>	0.076 <sup>+0.021</sup> <sub>-0.017</sub>	0.040 ± 0.006	0.040 ± 0.006	0.040 ± 0.006	PS
16	1.76 <sup>+0.14</sup> <sub>-0.13</sub>	1.76 <sup>b</sup>	1.76 <sup>b</sup>	1.76 <sup>b</sup>	0.041 <sup>+0.012</sup> <sub>-0.010</sub>	0.019 ± 0.003	0.019 ± 0.003	0.019 ± 0.003	PS
17	2.79 ± 0.17	2.79 <sup>b</sup>	2.79 <sup>b</sup>	2.79 <sup>b</sup>	0.183 <sup>+0.062</sup> <sub>-0.046</sub>	0.118 <sup>+0.017</sup> <sub>-0.016</sub>	0.118 ± 0.016	0.118 ± 0.016	PS

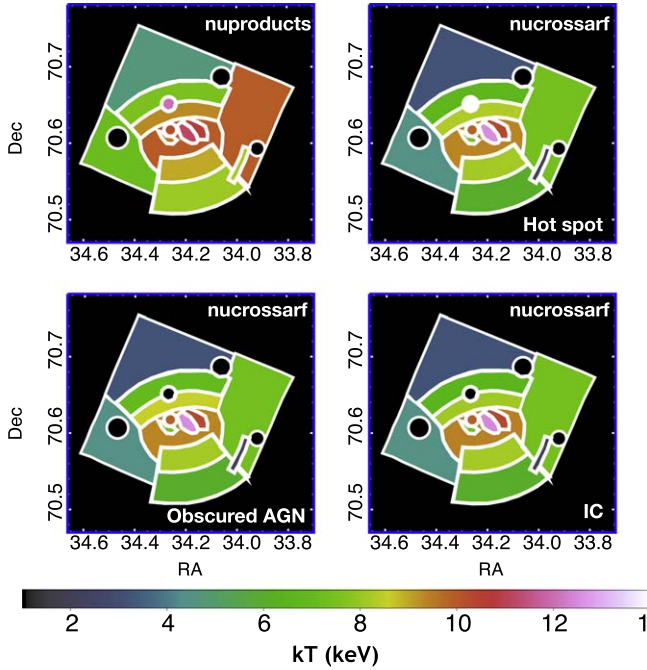
**Notes.** In the obscured AGN scenario, the value  $N_H$  is kept fixed at  $5.11 \times 10^{22} \text{ cm}^{-2}$ . apec normalization (norm) is given in  $\frac{10^{-14}}{4\pi(D_A(1+z))^2} \int n_e n_H dV$  ( $10^{-3} \text{ cm}^{-5}$ ) where power-law normalization ( $\kappa$ ) is photons  $\text{keV}^{-1} \text{ cm}^{-2} \text{ s}^{-1}$  at 1 keV ( $10^{-3}$ ).

<sup>a</sup> Lower limit.

<sup>b</sup> Photon indices are fixed to the nuproducts values.

<sup>c</sup> Upper temperature limit hits 9 keV.

<sup>d</sup> Upper norm limit hits  $1 \times 10^{-3} \text{ cm}^{-5}$ .



**Figure 7.** Temperature maps created with the results of nuproducts and nucrossarf analysis. We use the color black to fill in the regions where a power-law model is used to describe the data, that is, Regions 15, 16, and 17 for all maps, and Region 6 for obscured AGN and IC scenarios.

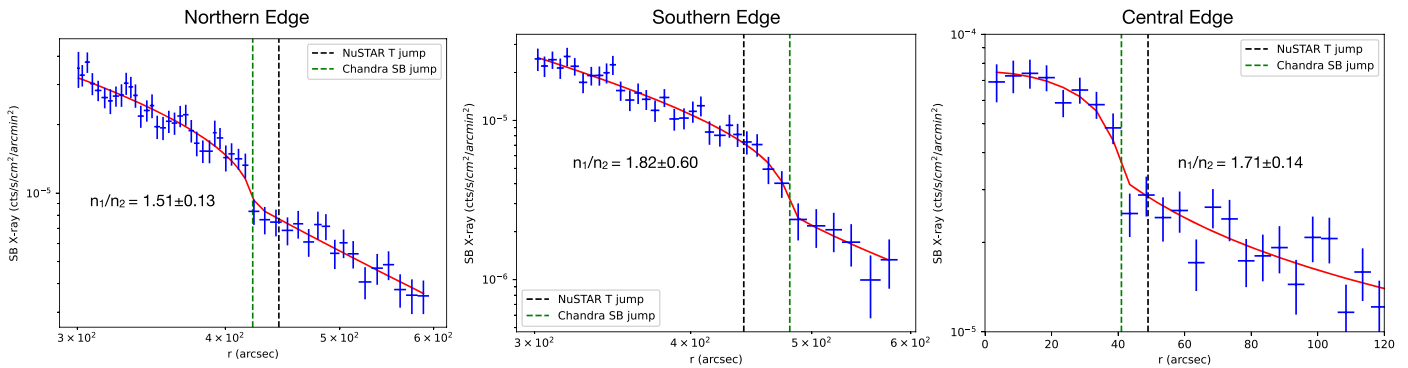
We then studied the Chandra SB profiles of the SB edges evidenced by NuSTAR, Chandra, LOFAR images, as well as our GGM analysis and temperature maps. These regions are 3–4 (C<sub>in</sub>–C<sub>out</sub>), 7–8 (N<sub>in</sub>–N<sub>out</sub>), and 9–10 (S<sub>in</sub>–S<sub>out</sub>), where the first region in these region couples are presumed post-shock and the second one represents the pre-shock.

Although Zhang et al. (2020b) study the SB profiles of northern and southern SB edges, we extracted new Chandra SB profiles from the exact regions used in this work for precision. The profiles and the best-fit models are shown in Figure 8. Assuming an adiabatic index of an ideal monoatomic gas of  $\gamma = 5/3$ , Mach numbers obtained from the density jumps are,  $\mathcal{M} = 1.35$ , 1.58, and 1.50 for the northern, southern, and central edges, respectively. The Mach numbers calculated by the temperature jumps from our cross-talk analysis range between 1.22 and 1.37. In addition, we calculated the Mach number for the temperature jump between regions 6–8, accounting for the possibility that the “hot spot” is in fact a hot plasma where the post-shock is localized at Region 6, i.e., a bullet-like feature, and Region 8 is the pre-shock region. This approach results in  $\mathcal{M} \sim 2$ . These Mach numbers are presented in Table 6.

The details of the nucrossarf analysis are presented in Appendix D.

### 3.5. Local Inverse Compton Search

We did not find strong evidence for extended IC emission from our global spectra fit results, but we continued to search



**Figure 8.** Chandra X-ray surface brightness profiles (blue) and the best-fit models (red) of the northern, southern, and central SB edges.

**Table 6**

Mach Numbers of Shock Fronts Calculated from the Temperature Jumps  
Obtained from the Cross-talk Results

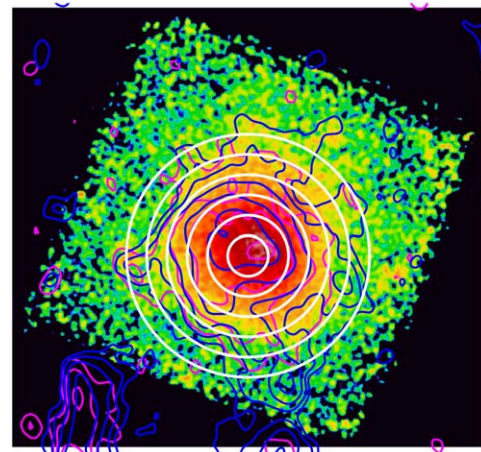
Regions		Mach Number		
Post-shock	Pre-shock	Hot spot	Obscured AGN	IC
3	4	1.22	1.22	1.21
6	8	2.01	...	...
7	8	1.24	1.23	1.24
9	10	1.37	1.37	1.37

for IC locally within the radio halo, with the motivation that IC flux may start to dominate the emission in narrower regions moving away from the center of the cluster where ICM dominates. For this analysis we used annular regions, where Hoang et al. (2021) studies radio spectral indices and we extracted NuSTAR spectra from five annuli as shown in Figure 9. Although six regions are selected by Hoang et al. (2021, Figure 7 therein) including a central circular region, we exclude that central region from our analysis expecting for the ICM to dominate the total emission; hence, we studied five annular regions. We applied the same analysis done for the NuSTAR global spectra to these annular spectra. We also allowed for metal abundances to be free. Model parameter results are shown in Table 7.

Annulus 1’s spectrum is best described by the single-temperature model, whereas for annuli 2–3–4, the 2T model describes the spectra the best-fit models. The outermost annulus, annulus 5, is best described by the 1T+IC model, but almost equally well as the 2T model does. This region roughly passes through Regions 8 and 10 of our cross-talk analysis.

#### 4. Summary and Discussion

CL 0217+70 hosts a giant radio halo and double radio relics, pointing to a late-stage merger. The location of radio relics points to a merger plane perpendicular to the line of sight. Motivated by the SB edges detected by Chandra (Zhang et al. 2020b) at the central region of the cluster, we observed the cluster with NuSTAR with the aim of studying the nature of these SB edges. We applied spectro-imaging methods using NuSTAR and Chandra data, and relying on the recent LOFAR study by Hoang et al. (2021).



**Figure 9.** Selected regions (white annuli) for IC search overlaid on NuSTAR 3.0–10.0 keV image. VLA L-band D configuration (magenta), at  $3\sigma_{\text{rms}} \times [1, 2, 4, 8]$  levels, where ( $\sigma_{\text{rms}} = 70 \mu\text{Jy beam}^{-1}$ ), and LOFAR (blue), at  $\sigma_{\text{rms}} \times [3, 6, 12, 24, 48]$ . ( $\sigma_{\text{rms}} = 330 \mu\text{Jy beam}^{-1}$  [ $46'' \times 45''$ ]) radio contours are also shown.

#### 4.1. Global View

We first studied the photon images of NuSTAR, Chandra, and LOFAR data. To capture any strong SB gradients, we used a GGM filter on the NuSTAR photon images, and we saw that an interesting SB edge feature consistently appears at the central region of the cluster with NuSTAR, Chandra, and LOFAR images as well as the NuSTAR GGM filter.

Background-extracted, exposure-corrected images (Figure 1) of NuSTAR and Chandra data point to a localized, enhanced emission at the central region, which we assigned as Region 3, for our cross-talk analysis (Figure 6). Furthermore, GGM and LOFAR images suggest a sharp edge between Regions 3 and 4, and the correspondence of this X-ray edge with the radio band, respectively, as seen in Figure 4.

In addition, NuSTAR images in the hard (10.0–20.0 keV) energy band hint at high temperature or the existence of nonthermal emission enclosed by the SB edges suggested by Zhang et al. (2020b) using Chandra data. We found that this hard excess is due to the hot ICM, given that we did not find a strong IC component. We do not directly detect a clear SB depression at the proposed (Zhang et al. 2020b) “channel” region from NuSTAR images.

The offset between the diffuse radio and X-ray central halo peak seen in the photon images (Figure 1), as well as the NuSTAR SB and radio contours overlaid on the temperature

**Table 7**  
IC Search Spectral Fit Results from Selected Annuli Shown in Figure 9

Annulus Number	Model	$kt$ (keV)	$Z_l$ ( $Z_\odot$ )	norm ( $10^{-3}$ )	$kt$ or $\Gamma$ keV or ...	norm or $\kappa$ ( $10^{-3} \text{ cm}^{-5}$ ) or ( $10^{-4}$ )	IC Flux	$C/\nu$
1	1T	$10.28^{+0.21}_{-0.20}$	$0.31 \pm 0.06$	$2.808^{+0.062}_{-0.061}$	...	...	...	1218.21 / 1318
	2T	$10.34^{+0.23}_{-0.21}$	$0.33^{+0.07}_{-0.06}$	$2.786^{+0.065}_{-0.067}$	$0.16^{+0.27}_{-0.13}$	$5.390\text{E}7^{+1.572\text{E}10}_{-5.401\text{E}7}$	...	1216.92 / 1316
	1T + IC	$10.28^{+0.25}_{-0.28}$	$0.31 \pm 0.07$	$2.373^{+0.102}_{-0.231}$	2.10 (fixed)	$0.300^{+0.880}_{-0.300}$	0.46	1218.21 / 1317
2	1T	$9.42^{+0.21}_{-0.20}$	$0.31 \pm 0.06$	$2.846^{+0.069}_{-0.068}$	...	...	...	1385.03 / 1365
	2T	$10.34^{+0.91}_{-0.54}$	$0.36 \pm 0.07$	$2.527^{+0.178}_{-0.371}$	$2.33^{+2.13}_{-1.02}$	$0.915^{+1.235}_{-0.423}$	...	1380.11 / 1363
	1T + IC	$8.90^{+0.37}_{-0.43}$	$0.38^{+0.08}_{-0.07}$	$2.384^{+0.239}_{-0.240}$	2.10 (fixed)	$1.853^{+0.937}_{-0.934}$	2.85	1381.48 / 1364
3	1T	$8.80^{+0.26}_{-0.27}$	$0.13 \pm 0.06$	$2.165^{+0.066}_{-0.065}$	...	...	...	1321.22 / 1351
	2T	$12.91^{+2.71}_{-2.78}$	$0.22^{+0.11}_{-0.08}$	$1.371^{+0.329}_{-0.294}$	$2.87^{+1.30}_{-1.64}$	$1.689^{+1.809}_{-0.334}$	...	1303.74 / 1349
	1T + IC	$6.84^{+0.68}_{-0.60}$	$0.24^{+0.09}_{-0.08}$	$1.464^{+0.163}_{-0.162}$	2.05 (fixed)	$2.842^{+0.611}_{-0.610}$	5.25	1306.49 / 1350
4	1T	$7.34^{+0.28}_{-0.27}$	$0.05^{+0.06}_{-0.05}$	$1.897^{+0.079}_{-0.078}$	...	...	...	1329.64 / 1361
	2T	$7.70^{+0.39}_{-0.33}$	$0.09^{+0.07}_{-0.06}$	$1.778^{+0.094}_{-0.102}$	$0.39^{+0.25}_{-0.16}$	$1.271\text{E}4^{+2.378\text{E}8}_{-1.319\text{E}4}$	...	1324.24 / 1359
	1T + IC	$7.23^{+0.37}_{-0.59}$	$0.05^{+0.06}_{-0.05}$	$1.837^{+0.89}_{-0.215}$	2.10 (fixed)	$0.231^{+0.841}_{-0.231}$	0.36	1329.53 / 1360
5	1T	$7.38 \pm 0.39$	$0.12 \pm 0.08$	$1.491^{+0.087}_{-0.079}$	...	...	...	1308.92 / 1435
	2T	$24.40^{+25.08}_{-15.63}$	$0.17^{+0.12}_{-0.08}$	$0.348^{+0.722}_{-0.193}$	$4.62^{+1.35}_{-2.57}$	$1.457^{+0.208}_{-0.546}$	...	1304.14 / 1433
	1T + IC	$5.55^{+1.01}_{-1.14}$	$0.26^{+0.19}_{-0.13}$	$0.975^{+0.228}_{-0.198}$	2.15 (fixed)	$2.300^{+0.798}_{-0.943}$	2.94	1304.25 / 1434

**Note.** Model norms are described in Table 2. IC flux is given for the 20.0–80.0 keV band in  $10^{-13} \text{ erg s}^{-1} \text{ cm}^{-2}$ .

map (Figure 5), is also observed by Brown et al. (2011) for this cluster, as well as in the Coma cluster by Deiss et al. (1997). This is thought to be due to the nonequilibrium state of the merger system (Brown et al. 2011).

Global analysis of the cluster constitutes the selection of a circular region (5'2) containing the radio halo (roughly enclosing Regions 1–9), extraction of spectra of this region from both NuSTAR and Chandra data, and fitting the spectra with single-temperature, two-temperature, and single-temperature-plus-nonthermal-emission models. The purpose of this analysis is to assess the global properties of the cluster and to search for possible extended IC emission in the cluster. Assuming an isothermal plasma, the global temperature found by NuSTAR is  $kT = 9.1 \pm 0.1 \text{ keV}$ , and for the joint NuSTAR and Chandra fit, we find  $kT = 9.2 \pm 0.3 \text{ keV}$ . The results of NuSTAR and joint NuSTAR and Chandra data analyses show that the statistics improve with an additional *apec* or power-law component, with respect to a single-temperature *apec* model. The power-law component was more dominant in the NuSTAR fit than the joint NuSTAR and Chandra fit, due to the bandpass of Chandra being narrower than that of NuSTAR. Therefore, the joint fit captures more of the thermal emission. The two-temperature model for the NuSTAR fit has a high-temperature component of  $T_H = 10.6^{+0.8}_{-0.4} \text{ keV}$  and a lower-temperature component with  $T_L = 2.2^{+1.1}_{-0.5} \text{ keV}$ . However, our further detailed analyses on the the temperature structure, i.e., temperature map and cross-talk analysis, do not show signs of dominant emission around this low-temperature value. Apparently, the multi-temperature structure of the cluster would theoretically be better described with a multi-temperature model, yet the temperature values of various regions within the radio halo being high and close to each other makes it statistically difficult to disentangle these components.

In the joint NuSTAR and Chandra fit, however, we witnessed a subtle high-temperature component of  $T_H = 21.56^{+2.71}_{-2.90} \text{ keV}$  and a dominant low-temperature component

of  $T_L = 6.4 \pm 0.4 \text{ keV}$ . The lower limit found for Region 6 for the hot-spot scenario in the cross-talk analysis results is actually within  $1\sigma$  of this global high-temperature component. The lower-temperature component, however, is too low with respect to what we see in the central region throughout this work, and also with respect to the findings of Zhang et al. (2020b, Table 1 therein). Overall, the statistics for both the NuSTAR and joint NuSTAR and Chandra fit were improved by adding a second *apec* model with  $\Delta C/\Delta\nu = 41.25/2$  and  $\Delta C/\Delta\nu = 36.96/2$ , respectively.

The addition of a power-law component to the single-temperature model improved the statistics by  $\Delta C/\Delta\nu = 38.3/1$  and  $\Delta C/\Delta\nu = 32.3/1$  for NuSTAR and joint NuSTAR and Chandra analysis, respectively. Statistically a 2T fits the data better than a 1T+IC description (Tables 2 and 3). The temperature component of the 1T+IC model is  $\sim 8 \text{ keV}$ . The NuSTAR and joint NuSTAR and Chandra analysis results agree within  $1\sigma$ .

Although the data are better described by the 2T model, we provide an IC flux only to report an upper limit, as if IC were detected. The power-law component was more dominant in the NuSTAR fit than that of the joint fit. Therefore, we use NuSTAR fit results for our flux calculations. The upper limit to the IC flux in the 20.0–80.0 keV band was calculated using the *cflux* model applied to the power law of the NuSTAR fit. The resulting flux is  $2.695 \times 10^{-12} \text{ erg s}^{-1} \text{ cm}^{-2}$ . Using the LOFAR data (Hoang et al. 2021), this refers to a lower limit of  $0.08 \mu\text{G}$  for the average magnetic field.

We also studied the effect of the  $N_H$  parameter on our global spectra results using priors from Zhang et al. (2020b). Since our global region radius is  $\sim 300''$ , the only prior we could use for  $N_H$  was fixing its value to  $8.21 \times 10^{21} \text{ cm}^{-2}$ , suggested by Zhang et al. (2020b), to test its impact on the global temperature and IC limit. By fixing the  $N_H$  to this value during the joint NuSTAR and Chandra 1T model fit, statistics become 2120.48/2108 d.o.f., where with free  $N_H$  it is 2104.29/2107 d.o.f. Between these two approaches, the global temperature



varies by 0.8%. Further, for the joint NuSTAR and Chandra 1T+IC model fit, fixing the  $N_H$  decreases the magnetic field lower limit by only 5% as opposed to letting it vary.

In addition, we studied the effect of the photon index,  $\Gamma$ , on the IC flux using our global joint NuSTAR and Chandra analysis (1T+IC model). We varied  $\Gamma$  between 1.9 and 2.1 from the fixed value of  $\Gamma = 2.0$ .  $\Gamma = 2.0$  is obtained from the spectral index ( $\alpha$ ) value in Hoang et al. (2021). The uncertainty given by Hoang et al. (2021) on this  $\alpha$  is  $\pm 0.05$ , and here we use a more conservative approach by taking the error as  $\pm 0.10$ . The IC flux changes by 9% and 12% by setting  $\Gamma = 1.9$  and  $\Gamma = 2.1$ , respectively, instead of  $\Gamma = 2.0$ .

#### 4.2. The “Hot Spot”

Our temperature map in Figure 5 shows a “hot spot” ( $\sim 12$  keV) at the location of the northern SB edge. We extracted NuSTAR spectra from this region to study the nature of the emission. We propose three scenarios to explain the emission from this source, which are (1) a hot spot where the shock-heated gas is concentrated at that region (bullet-like), (2) a highly obscured AGN, and (3) a localized IC emission connected to the radio source in the vicinity.

Shocks driven by a piston-like object, like a cool core, do not produce shocks with uniform Mach number across it, but will have higher Mach numbers near the piston and lower farther away. If the “hot spot” is actually of thermal origin, this would be a similar case as in the Bullet Cluster. If the shock surface is considered as a 2D sheet, the middle will have the highest Mach number (in this case,  $\mathcal{M} = 2$ ), and it will be lower everywhere else. At the hot spot–Region 8 interface the temperature jump will be highest and the particle acceleration will be most efficient.

Supported by theoretical and high-resolution hydrodynamical simulations (Gaspari et al. 2017, 2019), AGNs in massive hot halos often become heavily obscured via the CCA triggered by the top-down multiphase condensation of warm and cold clouds, which rain onto the central supermassive black hole. Such obscuring CCA rain has been also probed in lower-energy bands, e.g., with Atacama Large Millimeter/submillimeter Array and Multi Unit Spectroscopic Explorer absorption/emission-line features (Rose et al. 2019; Olivares et al. 2022; Temi et al. 2022).

However, at the “hot spot” location, there are no known AGNs. We also carried out a simple mid-IR selection criteria following Somboonpanyakul et al. (2022) using the All-WISE2020 Catalog.<sup>18</sup> Within  $r = 1'$  of the “hot spot” position, we found an IR object with ID J021703.24+703909.0 and found  $W1-W2 = -0.598$ . This value is much lower than what is expected from an AGN emission (Somboonpanyakul et al. 2022). However, we note that mid-IR selection for AGNs mostly select extremely bright AGNs (high accretion rate). This implies that the object may not be a strong AGN, but could still be a fainter/smaller AGN.

Furthermore, the vicinity of the radio galaxy may indeed be causing the IC emission due to the reacceleration of relativistic particles injected from the site or, by adiabatic compression, the merger shock may be “reenergizing” the radio plasma. The radio galaxy spectral index found by LOFAR is within  $1\sigma$  of the IC emission photon index we found.

Our NuSTAR analysis using `nuproducts` shows that all three scenarios are almost equally likely as represented in Table 4. However, the 2T model fit to the joint NuSTAR and Chandra data revealing a similar high temperature (Table 3) for the global assessment with the cross-talk results for Region 6 of the hot spot (Table 5) may not be a coincidence. Although we would expect NuSTAR to capture the higher-temperature component model better with respect to Chandra, the addition of the Chandra data may have helped to better constrain the lower-temperature model. Since Chandra data are quite shallow and foreground absorption is moderately high, it is difficult to make a conclusion.

#### 4.3. Cross-talk Analysis and Shock Fronts

To account for the scattering due to the NuSTAR PSF, we applied `nucrossarf` to dissociate the emission originating from a specific region from the other regions in the FOV. Our cross-talk analysis (Table 5) reveals several temperature jumps between the regions selected with the guidance of NuSTAR, Chandra, and LOFAR images, as well as temperature and GGM maps. These weak jumps occur at the Region 7–8 (northern) and 9–10 (southern), and the Region 3–4 (central) interfaces. We calculated Mach numbers for these jumps, and found  $\mathcal{M} = 1.22$ – $1.37$  (Table 6), hinting at multiple weak shocks within the radio halo. Our Chandra SB profiles show that these temperature jumps have corresponding density jumps with  $\mathcal{M} = 1.35$ – $1.58$ . The Mach numbers derived from the NuSTAR temperature jumps and Chandra density jumps found in this work are consistent with each other. The Mach number obtained for the density jumps from the southern SB edge detected by Zhang et al. (2020b) is  $2\sigma$  higher than what we find in this work. We reason that the shock may be the strongest (localized) at the center when a smaller angle sector is selected for the analysis, as we similarly discuss in the case of the hot spot scenario in Section 4.2.

The physical distances of the temperature (density) jumps are  $\sim 500$  ( $\sim 440$ ) kpc,  $\sim 650$  ( $\sim 780$ ) kpc, and  $\sim 100$  ( $\sim 72$ ) kpc from the emission peak center for the northern, southern, and central fronts, respectively. The difference between the locations of the temperature-density jumps may be due to the imperfect astrometry of NuSTAR, as well as the poor photon statistics of the Chandra data. Deeper Chandra observations could reveal more accurate and precise locations of the density jumps aided by Chandra GGM analysis followed by various deprojected radial SB profiles across the FOV.

On the technical side, we present a new code in this work, `nucrossarf`, aimed at accounting for the X-ray scattering in and out of spectral extraction regions within the NuSTAR FOV. We ran the code for three different scenarios for 17 sources, where the temperature and model normalization values of all sources are almost identical for the scenarios that point to the stability of the code. Furthermore, `nucrossarf` and `nuproducts` temperature values are in agreement within  $1\sigma$  for Regions 1–2–4–5–8–9 and  $2\sigma$  for Regions 3–7–10. Temperature values for Regions 11–12–13 that are at the outskirts of the cluster drop by  $\sim 2$  keV point to a contamination of hard excess from the point sources enclosed by them, which is supported by the fact that the normalizations of these point-source emissions are reduced by a factor of 2 after the cross-talk treatment. Region 6, the “hot spot”, and Region 14, the channel temperatures from `nuproducts`, are quite different from `nucrossarf` results.

<sup>18</sup> <https://irsa.ipac.caltech.edu/Missions/wise.html>



For the “channel” region, we see that the temperature and normalization parameters were poorly constrained. The scattered emission from the neighboring regions may be responsible for this instability, hinting at a very faint emission at the channel region.

The total fit C statistics for the cross-talk analyses are  $C/\nu = 14669.14/15218$ ,  $C/\nu = 14694.08/15219$ , and  $C/\nu = 14666.06/15218$  for the hot spot, obscured AGN, and IC scenarios that were assumed to explain the Region 6 emission, respectively. Although the best fit is obtained for the IC scenario, at this depth all scenarios are almost equally likely.

#### 4.4. IC Search

We also carried out a local search for IC for regions where radio spectral indices are given by Hoang et al. (2021) inside the radio halo. The outermost annulus fit results show that the 1T+IC model describes the spectra the best, but almost equally well with the 2T model. For this region, we find an upper limit of  $2.64 \times 10^{-13} \text{ erg s}^{-1} \text{ cm}^{-2}$  in the 20.0–80.0 keV band for the IC flux, if it were detected. This region, where the 1T+IC and 2T models have quite similar statistics, passes through Regions 8 and 10, that is, the outer region to the northern and southern shock fronts. Whereas annulus 3 has the highest IC flux, again it has similar statistics with the 2T model, and coincides with the northern and southern SB edges that are expected due to shock enhancement (see, e.g., Sarazin 2002).

### 5. Conclusion

Based on NuSTAR and Chandra data, complemented by a previous LOFAR study (Hoang et al. 2019), we studied the late-stage galaxy cluster merger CL 0217+70. We present our conclusions of this work in this section.

All three scenarios, namely, hot spot, obscured AGN, and localized IC emission, proposed for the “hot spot” captured by our temperature map seem to be equally likely. If the hot spot is indeed a thermal plasma of  $\sim 12$  keV, it indicates a shock front  $\sim 500$  kpc away from the cluster emission peak. For the obscured AGN or IC emission scenarios, deep optical and deep low-frequency radio observations are required to study the galaxy distribution at the site. In essence, what is witnessed here may even be a combination of a hot spot + IC.

We confirm two shock fronts at the Region 7–8 (northern) and 9–10 (southern) interfaces, as suggested by Zhang et al. (2020b), and detect another shock front at the Region 3–4 interface (central), within  $0.5 r_{500}$  of the cluster. The physical distances of the temperature (density) jumps are  $\sim 500$  ( $\sim 440$ ) kpc,  $\sim 650$  ( $\sim 780$ ) kpc, and  $\sim 100$  ( $\sim 72$ ) kpc from the emission peak center for the northern, southern, and central fronts, respectively. These weak shocks may be partially responsible for sustaining the giant radio halo emission by the (re) acceleration of the relativistic particles at the central region of the cluster.

The axes connecting these northern and southern secondary shock fronts are almost perpendicular to the axes connecting the radio relics, suggesting that these secondary shocks are unrelated to the first core passage. The coincidence of the northern and southern shock fronts with the radio halo emission edge adds this cluster to a short list of clusters that suggests the radio halos’ formation may be boosted by the turbulence formed directly behind shocks. Deeper high-angular-resolution X-ray observations should reveal  $\sim 100$  kpc scale turbulence

eddies, taking advantage of the merger plane lying perpendicular to the line of sight.

To the best of our knowledge, this cluster is the second known case where a secondary shock coinciding with the radio halo emission in the form of subsequent settling of the ICM has been observed within 1 Mpc, the first being Coma (Simionescu et al. 2013).

Unlike Coma, CL 0217+70 shows multiple shock fronts, which makes this cluster the *only* known case where multiple secondary shock fronts are formed within  $0.5 r_{500}$ . We may have captured this cluster before the settling of the ICM, hence further studies beyond local systems are needed to investigate the ubiquity of these secondary shocks to understand the evolution of galaxy cluster mergers and radio halo formation mechanisms. Galaxy clusters hosting giant radio halos can be the first place to look for similar cases.

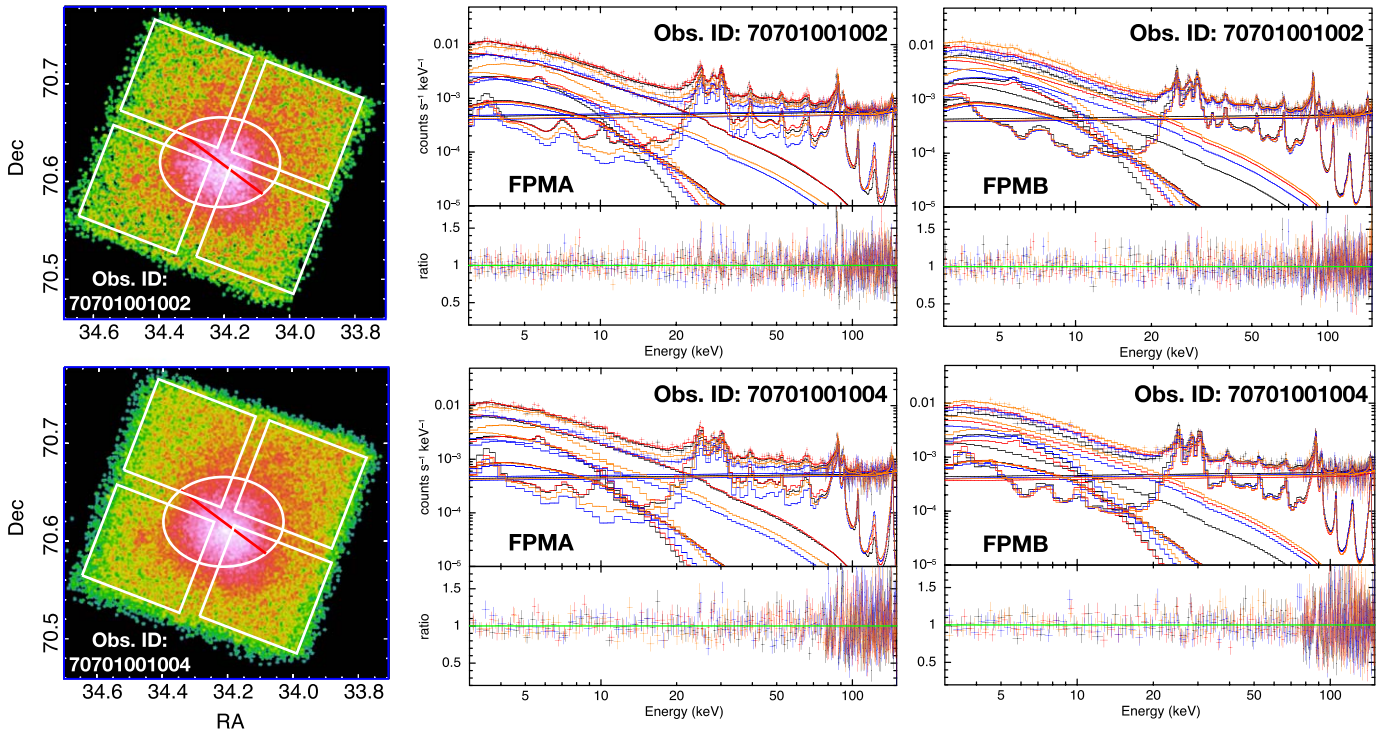
We thank the anonymous referee for valuable suggestions that improved our manuscript. A.T. and D.R.W. acknowledge support from NASA NuSTAR GO grant No. 80NSSC22K0066 and from NASA ADAP award No. 80NSSC19K1443. M.G. acknowledges partial support by NASA Chandra GO9-20114X and HST GO-15890.020/023-A, and the BlackHoleWeather program. R.J.v.W. acknowledges support from the ERC Starting Grant ClusterWeb 804208. C.S. acknowledges support from the MIUR grant FARE “SMS”. A.T. thanks Ross Silver and Taweewat Somboonpanyakul for valuable discussions. This research has made use of data from the NuSTAR mission, a project led by the California Institute of Technology, managed by the Jet Propulsion Laboratory (JPL), and funded by the National Aeronautics and Space Administration (NASA). In this work, we used the NuSTAR Data Analysis Software (NuSTARDAS) jointly developed by the ASI Science Data Center (ASDC, Italy) and the California Institute of Technology (USA). The data for this research have been obtained from the High Energy Astrophysics Science Archive Research Center (HEASARC), provided by NASA’s Goddard Space Flight Center. This research has also made use of data obtained from the Chandra Data Archive and the Chandra Source Catalog, and software provided by the Chandra X-ray Center (CXC) in the application package CIAO.

## Appendix A

### NuSTAR Background Assessment and Systematics

In this section, we present the spectra from the background model fits using both FPMs and both Obs. ID in Figure 10. As shown in the left panel of Figure 10, we selected four regions in the FOV from each detector chip, excluding the ICM emission as much as possible but also including as much data as available. Region selection is somewhat an experienced guess, and we tested the fits for smaller and larger regions to optimize the stability of the fit. The method is described in Wik et al. (2014).

In addition, we note that the single-temperature `apecc` model is sufficient to account for local and scattered cluster emission inside background regions, and more complicated models (e.g., two-temperature `apecc` model) do provide significant improvement. More importantly, the additional component, if not limited by strict priors, will generally try to model some other feature of the ICM spectra where the background model is not perfect.



**Figure 10.** Selected regions for background analysis (left panel) laid over cleaned NuSTAR 3–10 keV photon images. White squares indicate regions where the background spectra is extracted. Joint fit of background and cluster emission of NuSTAR FPMA (middle panel) and FPMB (right panel) for Obs. ID 70701001002 (upper panel) and Obs. ID 70701001004 (lower panel). Each color represents a region selected for the background fit. For plotting purposes, adjacent bins are grouped until they have a significant detection at least as large as  $15\sigma$ , with maximum 15 bins.

To quantify the systematics of the fCXB in the NuSTAR background analysis (Wik et al. 2014), we chose Region 5, which has the least complicated thermal structure. We increased and decreased the fCXB component of the background by 50% in the spectral fits to see its effect on the temperature measurements. We chose 50% since, given the cosmic variance for a region of this size, it is the expected variation in CXB that is also comparable to the brightness of the detected point sources. Increasing the fCXB component of the background by 50% resulted in a temperature decrease of 0.04 keV, whereas decreasing the fCXB component of the background by 50% resulted in a 0.06 keV increase in the temperature. These values correspond to less than 35% of the statistical errors on the temperature of that region.

The dominant systematic uncertainty of the NuSTAR background comes from the aperture cosmic X-ray background characterization, which dominates the  $E \sim 10$  keV background, but it is generally too flat to bias the thermal continuum and thus temperature measurements (Wik et al. 2014). This statement is less true when an IC model is included, but since the data do not support IC emission over pure thermal emission, the effect of this systematic uncertainty is negligible concerning our results.

### Appendix B NuSTAR and Chandra Global Fit Spectra

We present the results of the global spectral fit in this section for only NuSTAR and joint NuSTAR and Chandra data using the 1T, 2T, and 1T + IC models, as shown in in Figure 11. Since the statistics are quite similar, the differences in ratios are not discernible, yet the model contribution curves provide an insight to the contribution of different models.

### Appendix C “Hot Spot” Scenarios

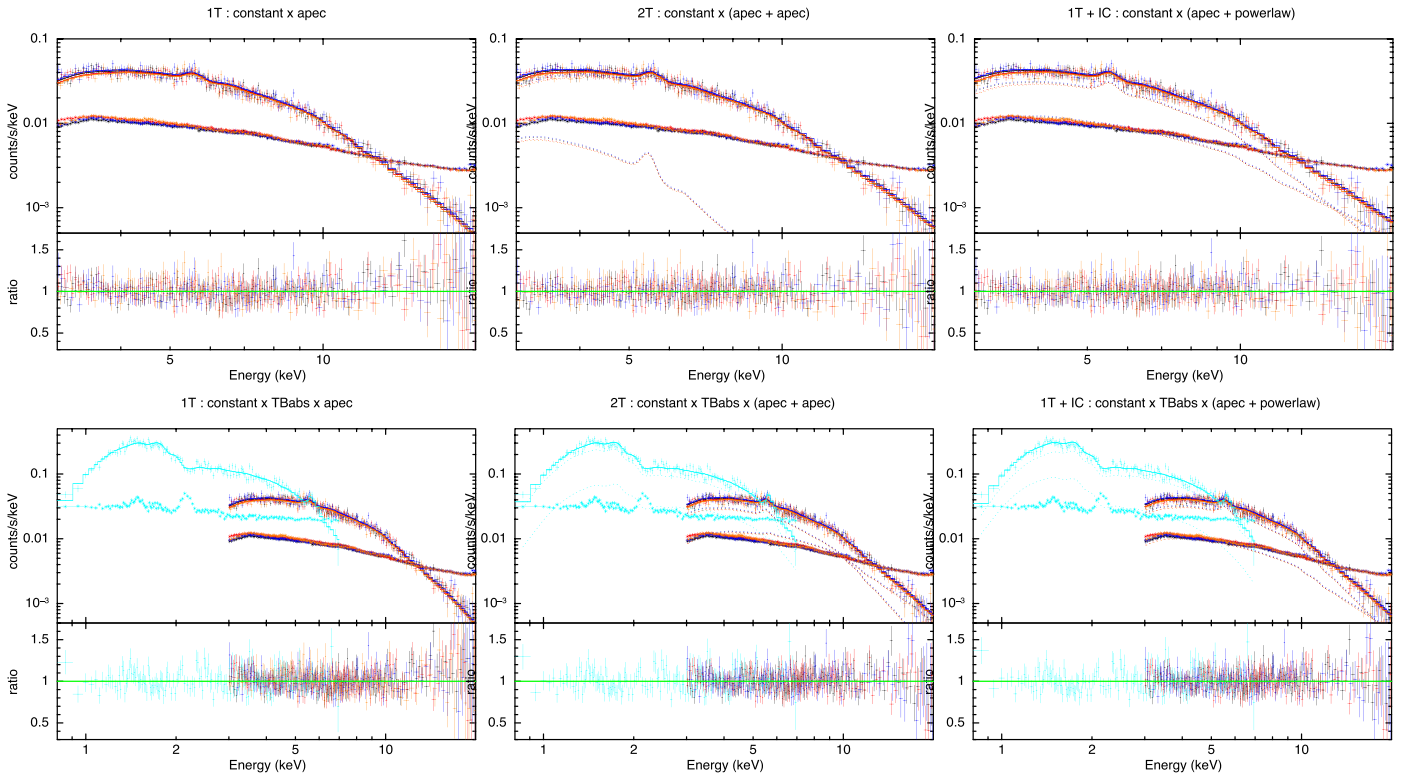
The resulting spectra from the three scenarios proposed for the explanation of the Region 6 emission is presented in this section. The statistics are again similar, which makes it difficult to conclude from the figures which model best describes the data. However, in its spectrum we encountered a strange dip around 4.8 keV in Figure 12. We extracted spectra from a larger ( $1'$ ) circular region at the location at the “hot spot”, as well as different data and plotting bins. The dip feature still persists for those spectra, as well, pointing to a reason different from a mere coincidence of statistical fluctuations. We could not find an explanation for this feature, and we refrain from any speculations.

### Appendix D Nucrossarf

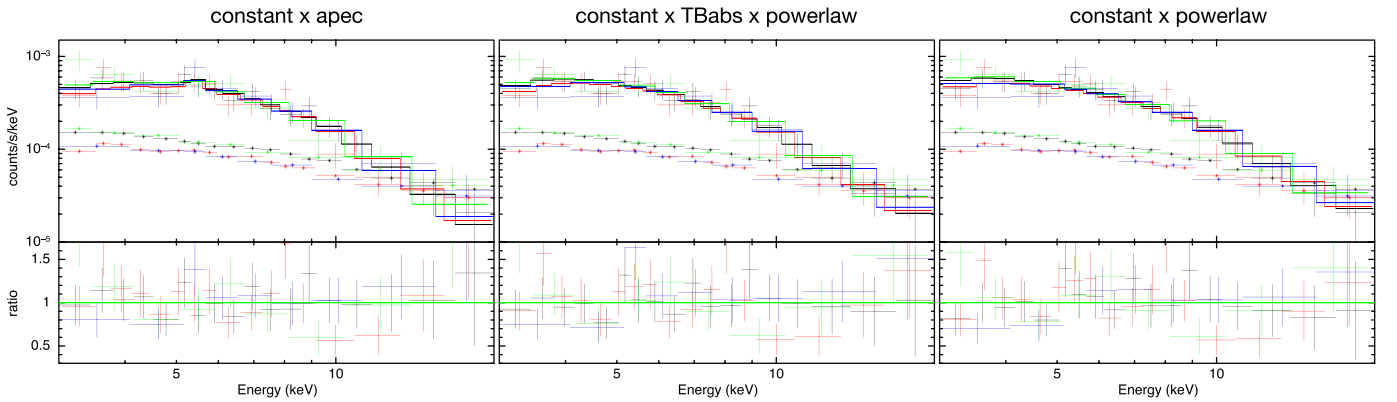
With this detailed study, we also happen to test the new `nucrossarf` code. In this section, we elaborate the inner workings of the code and what to expect from the code for future users.

`nucrossarf` mainly calculates the cross-ARFs of a number of user-defined extracted regions, and dissociates the source distribution from the contamination from other regions by jointly fitting the spectra of all regions. For  $N$  extracted regions, `nucrossarf` generates  $N \times N$  ARFs to account for the wings of the PSF of each source present in other regions.

The final fitted spectra for the obscured AGN scenario is presented in the left panel of Figure 13 as an example. This figure shows the spectra from each source, the total ARF curve, and the individual contributions from all regions, for two



**Figure 11.** Global fits of NuSTAR (upper panel), and joint NuSTAR and Chandra data (lower panel) with 1T (left panel), 2T (middle panel), and 1T + IC (right panel) of the spectra extracted from the central  $5/2$  circular region. Black indicates FPMA and red indicates FPMB for ObsID 70701001002, whereas for ObsID 70701001004, FPMA and FPMB are indicated by blue and orange, respectively. Chandra ACIS-I is indicated by turquoise. The data and models are shown as the higher curve and lower lines correspond to background spectrum. The dashed curves correspond to the model components to visualize their contribution to the composed model. The “ratio” panel shows data-to-model ratios describing the goodness of the fit. For plotting purposes, adjacent bins are grouped until they have a significant detection at least as large as  $8\sigma$ , with maximum 12 bins.



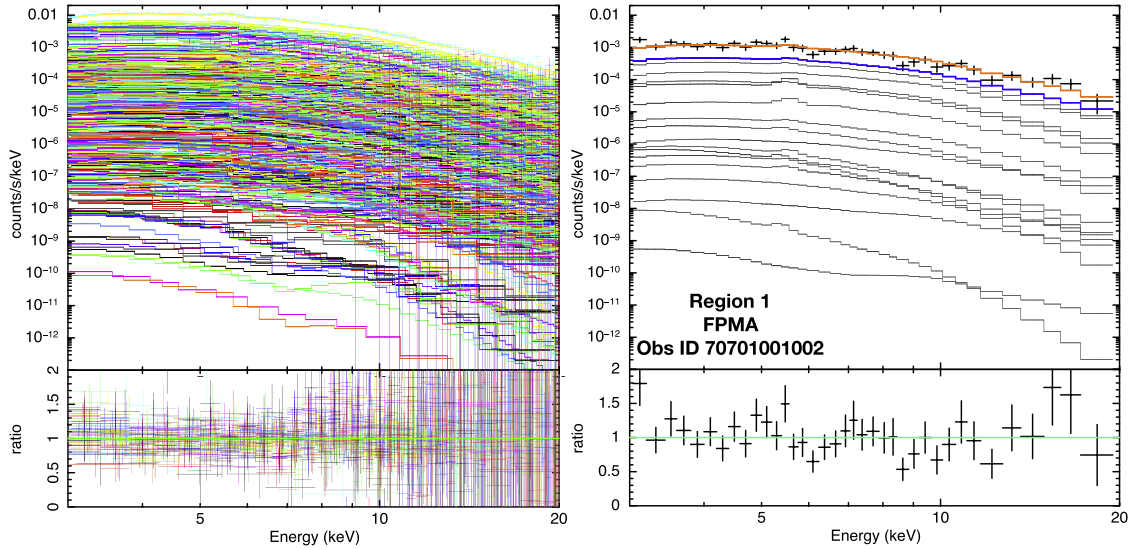
**Figure 12.** Spectra of the NuSTAR “hot spot” region fits with  $\text{constant} \times \text{apec}$  (left panel),  $\text{constant} \times \text{TBabs} \times \text{powerlaw}$  (middle panel), and  $\text{constant} \times \text{powerlaw}$  (right panel). Black indicates FPMA and red indicates FPMB for ObsID 70701001002, whereas for ObsID 70701001004, FPMA and FPMB are indicated by green and blue, respectively. For plotting purposes, adjacent bins are grouped until they have a significant detection at least as large as  $4\sigma$ , with maximum eight bins.

observations and for both FPMA and FPMB:  $(1 + 1 + 17) \times 2 \times 2$  curves in total. In order to present a much less complicated version, we plotted the spectrum from Region 1, the total ARF curve, and the individual contributions from all regions to Region 1 emission, for Obs ID 70701001002 and for FPMA as seen in the right panel of Figure 13.

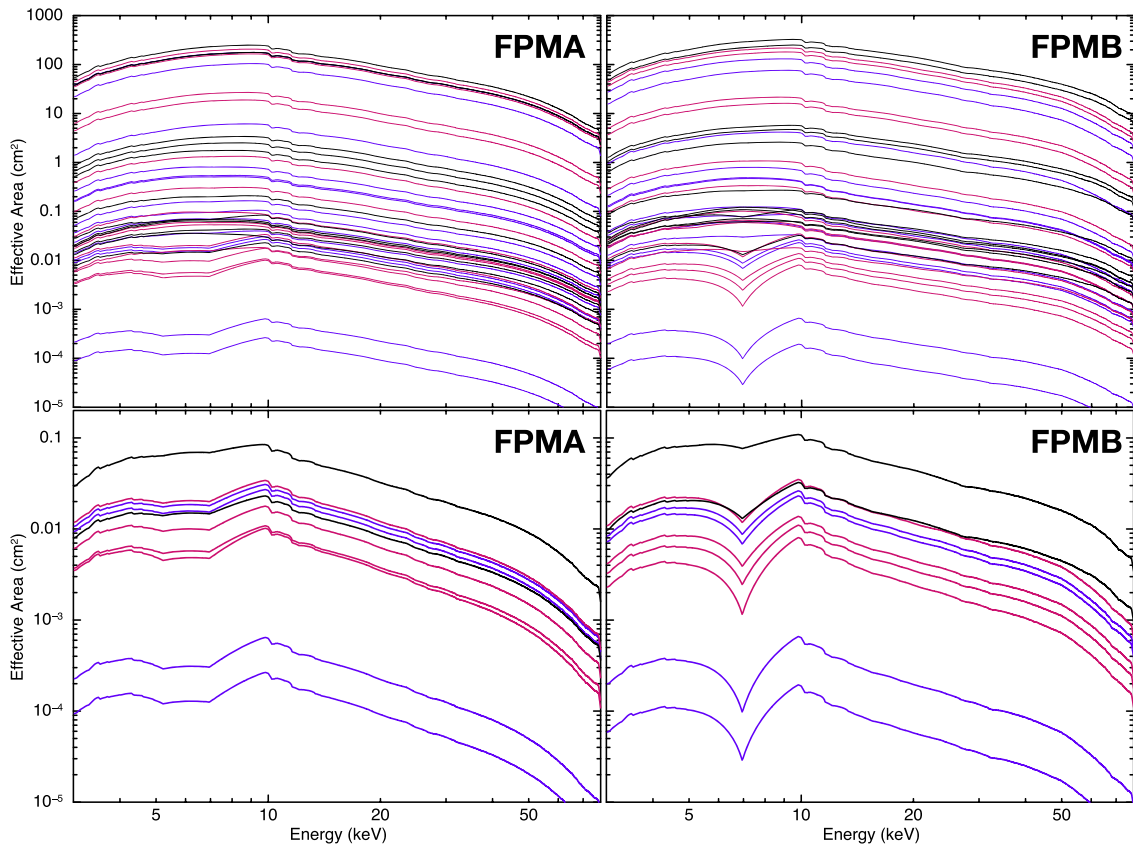
As seen in the `nucrossarf` spectral fit of Region 1 spectra for ObsID 70701001002 FPMA, the shape of the weakest model seen in the right panel in Figure 13 has an artifact, a dip within 5.0–10.0 keV. This model corresponds to the scattering from Region 17 to Region 1. We further investigated the

spectra for similar artifacts and saw that point source cross-talk contributions to the regions that are far away from these sources show a similar behavior. These curves are 15–10, 15–4, 16–2, 16–9, 16–14, 16–17, 17–1, 17–2, 17–12, and 17–16, where the first number in the couples points to the origin of the scattered light and the second corresponds to where the scattered light reaches. These cross-ARFs with artifacts for Obs ID 70701001002 are plotted in the lower panel of Figure 14, where the upper panel shows the entirety of the ARFs.





**Figure 13.** Total cross-talk spectra for the AGN scenario final fit (left panel) and the spectra for the AGN scenario, for Region 1, ObsID 70701001002 FPMA (right panel). In the right panel, black indicates the data, orange presents the total model, the blue curve is the local contribution model from Region 1, and gray curves represent the scattering from other regions.



**Figure 14.** All cross-ARFs for Regions 15 (black), 16 (purple), and 17 (pink) from Obs ID 70701001002 (upper panel), and only the cross-ARFs of artifacts (lower panel), namely cross-ARFs: 15-10, 15-4, 16-2, 16-9, 16-14, 16-17, 17-1, 17-2, 17-12, and 17-16.





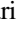









Since for the production of ARFs the PSF images at various bands are used, these artifacts are bound to happen for faint point sources that are close to the edge of the FOV where the calibration for the PSF is less than perfect. `nucrossarf` samples the PSF images for extended sources, therefore

averaging out very small fluctuations. Therefore we do not see any similar artifacts from Region 14, the channel, which is also close to the edge of the FOV and has faint emission. At very low effective area, the level of the artifacts are comparable to data noise. We emphasize that, at this rate, ARF



contributions where we see the dip artifact are effectively zero ( $\sim 10^{-9}$  counts  $s^{-1}$ ) and the artifacts do not have an effect on any of our results.

### ORCID iDs

Ayşegül Tümer  <https://orcid.org/0000-0002-3132-8776>  
 Daniel R. Wik  <https://orcid.org/0000-0001-9110-2245>  
 Xiaoyuan Zhang  <https://orcid.org/0000-0001-9110-2245>  
 Duy N. Hoang  <https://orcid.org/0000-0002-8286-646X>  
 Massimo Gaspari  <https://orcid.org/0000-0003-2754-9258>  
 Reinout J. van Weeren  <https://orcid.org/0000-0002-0587-1660>  
 Lawrence Rudnick  <https://orcid.org/0000-0001-5636-7213>  
 Chiara Stuardi  <https://orcid.org/0000-0003-1619-3479>  
 François Mernier  <https://orcid.org/0000-0002-7031-4772>  
 Aurora Simionescu  <https://orcid.org/0000-0002-9714-3862>  
 Randall A. Rojas Bolivar  <https://orcid.org/0000-0002-8882-6426>  
 Ralph Kraft  <https://orcid.org/0000-0002-0765-0511>  
 Hiroki Akamatsu  <https://orcid.org/0000-0003-1949-7005>  
 Jelle de Plaa  <https://orcid.org/0000-0002-2697-7106>

### References

- Abell, G. O. 1958, *ApJS*, **3**, 211
- Planck Collaboration, Ade, P. A. R., Aghanim, N., et al. 2013, *A&A*, **554**, A140
- Brown, S., Duisterhoeft, J., & Rudnick, L. 2011, *ApJL*, **727**, L25
- Brown, S., & Rudnick, L. 2011, *MNRAS*, **412**, 2
- Brunetti, G., Blasi, P., Reimer, O., et al. 2012, *MNRAS*, **426**, 956
- Brunetti, G., & Jones, T. W. 2014, *IJMPD*, **23**, 1430007
- Cash, W. 1979, *ApJ*, **228**, 939
- Cassano, R., Etori, S., Giacintucci, S., et al. 2010, *ApJL*, **721**, L82
- Clavico, S., De Grandi, S., Ghizzardi, S., et al. 2019, *A&A*, **632**, A27
- Cova, F., Gastaldello, F., Wik, D. R., et al. 2019, *A&A*, **628**, A83
- De Grandi, S., Eckert, D., Molendi, S., et al. 2016, *A&A*, **592**, A154
- Deiss, B. M., Reich, W., Lesch, H., & Wielebinski, R. 1997, *A&A*, **321**, 55
- Eckert, D., Gaspari, M., Vazza, F., et al. 2017, *ApJL*, **843**, L29
- Ensslin, T. A., Biermann, P. L., Klein, U., & Kohle, S. 1998, *A&A*, **332**, 395
- Feretti, L., Giovannini, G., Govoni, F., & Murgia, M. 2012, *A&ARv*, **20**, 54
- Gabici, S., & Blasi, P. 2003, *ApJ*, **583**, 695
- Gaspari, M. 2015, *MNRAS*, **451**, L60
- Gaspari, M., & Churazov, E. 2013, *A&A*, **559**, A78
- Gaspari, M., Eckert, D., Etori, S., et al. 2019, *ApJ*, **884**, 169
- Gaspari, M., Ruszkowski, M., & Oh, S. P. 2013, *MNRAS*, **432**, 3401
- Gaspari, M., Temi, P., & Brighenti, F. 2017, *MNRAS*, **466**, 677
- Gaspari, M., Tombesi, F., & Cappi, M. 2020, *NatAs*, **4**, 10
- Giles, P. A., Maughan, B. J., Pacaud, F., et al. 2016, *A&A*, **592**, A3
- Giovannini, G., & Feretti, L. 2004, *JKAS*, **37**, 323
- Harrison, F. A., Craig, W. W., Christensen, F. E., et al. 2013, *ApJ*, **770**, 103
- Hlavacek-Larrondo, J., Gendron-Marsolais, M.-L., Fecteau-Beaucage, D., et al. 2017, *MNRAS*, **475**, 2743
- Hoang, D. N., Shimwell, T. W., van Weeren, R. J., et al. 2019, *A&A*, **622**, A20
- Hoang, D. N., Zhang, X., Stuardi, C., et al. 2021, *A&A*, **656**, A154
- Hofmann, F., Sanders, J. S., Nandra, K., Clerc, N., & Gaspari, M. 2016, *A&A*, **585**, A130
- Markevitch, M., Ponman, T. J., Nulsen, P. E. J., et al. 2000, *ApJ*, **541**, 542
- Markevitch, M., Sarazin, C. L., & Vikhlinin, A. 1999, *ApJ*, **521**, 526
- Maslowski, J. 1972, *AcA*, **22**, 227
- Olivares, V., Salome, P., Hamer, S. L., et al. 2022, *A&A*, **666**, A94
- Reiprich, T. H., Basu, K., Etori, S., et al. 2013, *SSRv*, **177**, 195
- Rojas Bolivar, R. A., Wik, D. R., Giacintucci, S., et al. 2021, *ApJ*, **906**, 87
- Rose, T., Edge, A. C., Combes, F., et al. 2019, *MNRAS*, **489**, 349
- Ryu, D., Kang, H., Hallman, E., & Jones, T. W. 2003, *ApJ*, **593**, 599
- Sanders, J. S., Fabian, A. C., Russell, H. R., Walker, S. A., & Blundell, K. M. 2016, *MNRAS*, **460**, 1898
- Sarazin, C. L. 2002, in *Merging Processes in Galaxy Clusters*, ed. L. Feretti, I. M. Gioia, & G. Giovannini, Vol. 272 (Dordrecht: Kluwer Academic), 1
- Schellenberger, G., David, L., O'Sullivan, E., Vrtilak, J. M., & Haines, C. P. 2019, *ApJ*, **882**, 59
- Shimwell, T. W., Brown, S., Feain, I. J., et al. 2014, *MNRAS*, **440**, 2901
- Simionescu, A., Werner, N., Urban, O., et al. 2013, *ApJ*, **775**, 4
- Smith, R. K., Brickhouse, N. S., Liedahl, D. A., & Raymond, J. C. 2001, *ApJL*, **556**, L91
- Somboonpanyakul, T., McDonald, M., Noble, A., et al. 2022, *AJ*, **163**, 146
- Temi, P., Gaspari, M., Brighenti, F., et al. 2022, *ApJ*, **928**, 150
- van Weeren, R. J., Brunetti, G., Brügggen, M., et al. 2016, *ApJ*, **818**, 204
- van Weeren, R. J., de Gasperin, F., Akamatsu, H., et al. 2019, *SSRv*, **215**, 16
- Vikhlinin, A., Burenin, R. A., Ebeling, H., et al. 2009, *ApJ*, **692**, 1033
- Wik, D. R., Hornstrup, A., Molendi, S., et al. 2014, *ApJ*, **792**, 48
- Wik, D. R., Sarazin, C. L., Finoguenov, A., et al. 2011, *ApJ*, **727**, 119
- Wittor, D., & Gaspari, M. 2020, *MNRAS*, **498**, 4983
- Yang, H. Y. K., Gaspari, M., & Marlow, C. 2019, *ApJ*, **871**, 6
- Zhang, C., Churazov, E., Dolag, K., Forman, W. R., & Zhuravleva, I. 2020a, *MNRAS*, **498**, L130
- Zhang, X., Simionescu, A., Kaastra, J. S., et al. 2020b, *A&A*, **642**, L3